Bivariate 2D Empirical mode decomposition for analyzing instantaneous turbulent velocity field in unsteady flows Experiments in Fluids

Mehdi Sadeghi, Fabrice Foucher, Karim Abed-Meraim, Christine Mounaïm-Rousselle

Bivariate 2D empirical mode decomposition for analyzing instantaneous turbulent velocity field in unsteady flows

Mehdi Sadeghi, Fabrice Foucher, Karim Abed-Meraim, Christine Mounaïm-Rousselle

Laboratoire PRISME, Université d'Orléans, 8 rue Léonard de Vinci, 45072 Orléans, France

We introduce and demonstrate the bivariate two-dimensional empirical mode decomposition (bivariate 2D-EMD) for the decomposition of a turbulent instantaneous velocity field to separate spatial large-scale organized motion from random turbulent fluctuations. To validate this approach, it was applied to an experimental homogeneous and isotropic turbulent flow (HIT), perturbed by a synthetic Lamb–Oseen vortex that mimics the feature of organized motion. Through different test cases, the scale, the amplitude and the position of the synthetic vortex with respect to the turbulent velocity field were changed. By applying an energy criterion on the modes which resulted from the decomposition process, the initial HIT flow was separated from synthetic perturbation. It is important to point out that in this approach the decomposition as well as the distinction of different parts of the flow are free from any prior and objective assumptions and it requires just one instantaneous velocity field of the flow under analysis. The proposed methodology could be used for analyzing 2D velocity fields obtained from experimental measurement or CFD in different configurations (in-cylinder flow, channel flows, etc.).

1 Introduction

Ever since the existence of so-called coherent structures in turbulent flow was observed (Brown and Roshko 1974), their identification, characterization and separation from background turbulence have become a topic of major interest in the scientific community (Epps 2017). Due to their considerable content of flow energy (Fiedler 1998), they have a great influence on several physical phenomena such as mixing processes, combustion, heat transfer, noise generation, and fluid–structure interaction. While the coherent structures are significantly persistent in time and space, their definition is not universal and is open to debate (Hussain 1983; Bonnet et al. 1998). In the triple decomposition introduced by Reynolds and Hussain (1972), a physical variable of turbulent flow such as the instantaneous velocity U is separated into a mean $\bar{u}$ (i.e., time-averaged), a coherent part u^{c} (i.e., ensemble or phase-averaged component) and a random fluctuation u^{r}, so $U = \bar{u} + u^{\mathrm{c}} + u^{\mathrm{r}}$. However, in this definition, no correlation between the coherent and the turbulent part is considered. Such a decomposition is not straightforward and several approaches were proposed to distinguish different parts of the velocity field in turbulent flow. Traditional Fourier-based analysis (harmonic decomposition with fixed frequencies), for instance, can be used to separate flow organized motion from small scales. It is efficient

when a well-identified typical frequency exists within the data. Nevertheless, the choice of the cut-off frequency for scale separation is a major drawback of this method. In addition, such an analysis can only give a meaningful interpretation to linear and stationary processes and its application to nonlinear and nonstationary processes is problematic (Huang et al. 1998). Another attractive method called proper orthogonal decomposition (POD) was suggested by Lumley (1967) to extract coherent structures from turbulent flow. This method was developed in the signal processing community by Pearson (1901) and Hotelling (1933), and named Principal Component Analysis (PCA). It is a linear procedure that decomposes the velocity field into a set of orthogonal basis functions (i.e., modes) chosen according to their energy level. Afterwards, the separation between the contributions of the coherent part, the first energetic modes, and random fluctuations is performed by truncating the series of the modes, which requires defining an objective criterion (Druault et al. 2005; Roudnitzky et al. 2006; Foucher et al. 2008). In addition, the POD method is a statistical approach associated with a convergence criterion that restricts its interest in the case of intrinsically transient flows. A more sophisticated filtering method, the wavelet transform, can be used to extract coherent structures from the turbulent fluctuating field as proposed by Farge et al. (1999, 2001) and Lewalle et al. (2000). In this approach, the signal is represented in terms of prior basis functions (mother wavelet), that is, non-adaptive nature of wavelet decomposition; hence, the performance of the analysis is closely tied to how well the morphology of the signal under study is represented by these selected basis elements. It should be pointed out that this method was originally designed to process nonstationary but linear phenomena (Strang 1989; Flandrin 1998). For the analysis of nonstationary and nonlinear data, Huang et al. (1998) introduced the empirical mode decomposition (EMD) method, which is intuitive, direct, and adaptive with a posteriori-defined basis derived from data. The combination of the EMD and Hilbert spectral analysis (HSA) to obtain the instantaneous frequency, designated as the Hilbert Huang transform (HHT) gives the time–frequency–energy representation for nonlinear and nonstationary data. The decomposition is based on the simple assumption that at any given time, the data may have many different coexisting oscillatory modes, with significantly different frequencies, one superimposed on the others. EMD can provide the decomposition of any complicated data set into a finite and often small number of simple intrinsic oscillatory modes, also called intrinsic mode functions (IMFs). An IMF is a counterpart

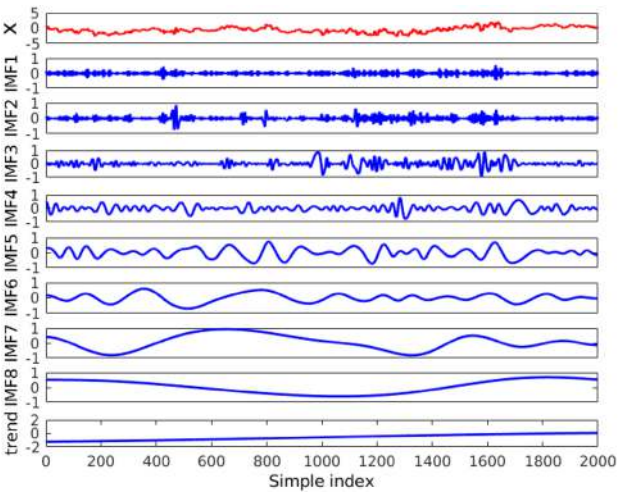

Fig. 1 EMD analysis of a turbulent signal in the top panel and the corresponding IMFs (modes)

to the simple harmonic function but instead of constant amplitude or frequency, as in the case of dynamical mode decomposition (Schmid 2010), it has both variable amplitude and frequency as a function of time, i.e., a multiscale function. Given a one-dimensional (1D) signal, the algorithm of EMD is described as follows:

1. Identify all local extrema of the variable $x(t)$.
2. Interpolate (using local spline interpolation) between all the minima (resp. maxima) to obtain the signal envelope passing through the minima, $e_{\min}(t)$ (resp. $e_{\max}(t)$).
3. Compute the local mean $m(t) = \left(e_{\min}(t) + e_{\max}(t)\right)/2$.
4. Subtract the local mean from the signal to obtain the modulated oscillation, local detail $h(t) = x(t) - m(t)$.
5. The component $h(t)$ is then examined to check if it satisfies the condition to be an IMF (given below). If yes it is considered as the first IMF and denoted $\mathrm{IMF}_1 = h(t)$, else set $x(t) = h(t)$ and go to step 1.
6. Subtract the so-derived IMF from the variable $x(t)$ so that the residual, $r(t) = x(t) - \mathrm{IMF}(t)$, is taken as the new data series in step 1.
7. Stop the process when the residual from step 6 becomes a monotonic function, i.e., signal trend, from which no more IMFs can be extracted.

In EMD procedure, step 1 to step 5 is called the sifting process that iterates until the detail $h(t)$ satisfies the following conditions to be an IMF. First, from the whole data set the number of extrema and zero crossings are either equal or differ by exactly one. Second, at any point, the mean value of the envelope defined by the local maxima and the envelope

defined by the local minima is zero (symmetric upper/lower envelope).

Several stoppage criteria were proposed by different investigations which are not discussed here, but a general discussion about all the criteria can be found in Wang et al. (2010). After decomposition, the input signal can, therefore, be expressed as $x(t) = \sum_{k=1}^{N} \mathrm{IMF}_k + r_N(t)$. In this way, EMD decomposes gradually any arbitrary signal from the finest scale of the shortest period to longer ones. As an example, Fig. 1 presents the analysis of a turbulent velocity signal (first line) by EMD and its corresponding IMFs.

EMD has been exhaustively tested and validated (Huang and Attoh-Okine 2005) and has met with great success in various scientific fields such as seismology (Zhou et al. 2012) and geophysics (Feynman and Ruzmaikin 2014), biology (Liang et al. 2005), atmospheric physics (Franzke 2014) and brain–computer interface (Wu et al. 2011; Hemakom et al. 2016). Huang et al. (1999) used EMD and the Hilbert transform to assess the evolution of Stokes and nonlinear water waves. They demonstrated the advantages of this approach as compared to wavelet decomposition for the identification of different events in the velocity field. Huang et al. (2008) applied EMD on homogenous turbulence time series to investigate turbulent scaling intermittency. Ducoin et al. (2009) applied EMD to analyze the temporal evolution of turbulent flow pressure over a transient moving hydrofoil. Foucher and Ravier (2010) determined turbulence properties on a random perturbed flow and Mazellier and Foucher (2011) used EMD to separate coherent structures from random turbulent fluctuations. Sadeghi et al. (2016) applied bivariate EMD to separate coherent structures from interference fluctuations in turbulent flow.

All these applications are limited to the temporal analysis of the local velocity field at one point in the flow. EMD has also been applied on two-dimensional data during the last decade. Bidimensional EMD has proved remarkably successful in image processing (Linderhed 2009; Looney and Mandic 2009) and pattern recognition (Nunes et al. 2005; Guanlei et al. 2009). However, to the best of our knowledge, EMD analysis has not yet been developed in the signal processing community for the decomposition of bivariate (i.e., two components)-2D signals such as the 2D velocity fields in which the velocity vector has two components, i.e., horizontal and vertical velocities.

The objective of this study is to extend the EMD method to the decomposition of bivariate two-dimensional signals to separate flow large-scale organized structures from turbulent random fluctuations in 2D fields. Since EMD is developed to process nonlinear and nonstationary phenomena, such an approach is entirely appropriate for analyzing flows that are inherently unsteady. For instance, it can be applied on instantaneous in-cylinder velocity fields of thermal engines to study the large-scale cycle-to-cycle variation of the gas motion that has a significant impact on engine performance (see Borée and Miles 2014 for a recent review). It can also be used to estimate the turbulent fluctuations near piston top-dead-center that have a great influence on flame propagation and the combustion process (Lumley 2001). The paper is organized as follows. Section 2 is dedicated to the description of the temporal (1D) multivariate EMD. Section 3 presents the description of the proposed bivariate 2D-EMD. The potential of this approach in the decomposition of turbulent velocity fields and the methodology used to separate the large-scale organized motion from the random turbulent field are presented in Sect. 4. The main results and concluding remarks are provided in Sect. 5.

2 Multivariate EMD

The key issue for extending standard EMD to process one-dimensional multivariate signals is the definition of the local mean since the definition of extrema for multivariate signals is not obvious. The bivariate signal can be considered as a complex-valued signal so to define the extrema envelopes, it should be projected in a given set of uniformly distributed directions in the complex plane, $\varphi_k = 2k\pi/N$ with $1 \leq k \leq N$. Then the periphery of the envelope is the signal extrema in each direction. The interpolation, cubic spline, of extrema in each direction ends up with the partial envelope curve in direction φ_k, for more details, see Rilling et al. (2007).

Inspired by this idea, the Trivariate EMD was developed by Rehman and Mandic (2010); in this method, the extrema are found by projecting the input signal in multiple directions in 3D space using quaternion rotation framework. A unite quaternion vector is written as $q = \cos\theta + \mathbf{u}\sin\theta = e^{\mathbf{u}\theta/2}$, where $\mathbf{u}$ is a 3D vector of unit length. So $B^{'}$ the rotation of a 3D vector B about $\mathbf{u}$ by angle 2θ is defined using $B^{'} = qBq^{*} = e^{\mathbf{u}\theta/2} \cdot B \cdot \left(e^{\mathbf{u}\theta/2}\right)^{*}$, where the symbol "*" denotes the quaternion conjugate. Therefore, to obtain the signal rotations in 3D space, it needs generating a set of values of $\mathbf{u}$ and θ (multiple direction vectors). Each direction vector can be represented by a point on the surface of unit sphere (that is the end point of the unit vector drawn from the sphere center), so a set of direction vectors that represents the rotation axis $\mathbf{u}$ and the rotation angle θ is represented by several points at one longitudinal line of a unit sphere as shown in Fig. 2a. To project a signal on the whole 3D space, different equi-distance longitudinal lines on the sphere should be considered, presented in Fig. 2b, each

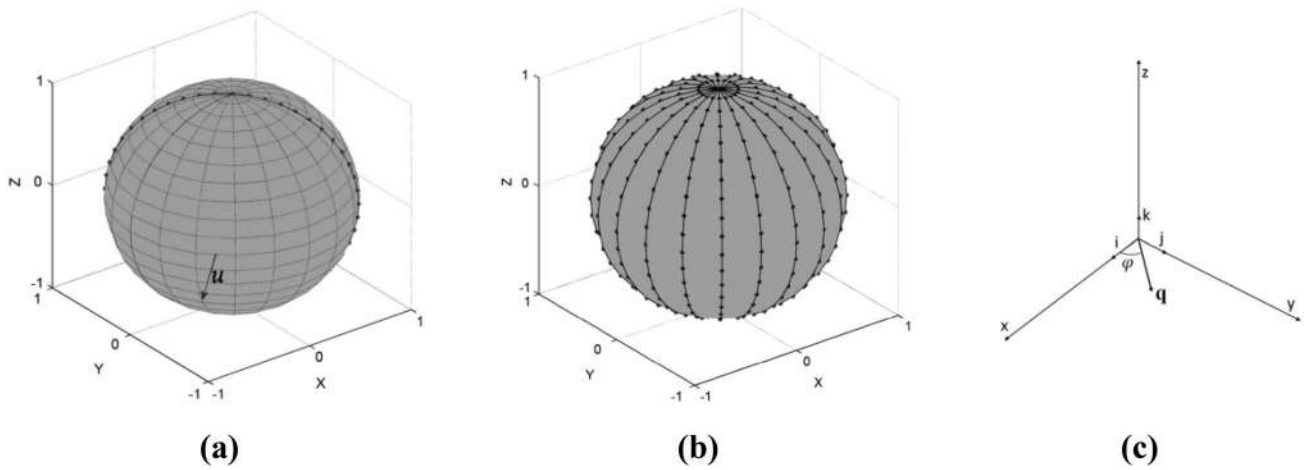

Fig. 2 **a** Multiple direction vectors on a single longitudinal line, corresponding to rotation axis u; b A set of multiple direc-tions vector spanning the whole 3D space; c Quaternion vector $\boldsymbol{q} = 0 + \cos(\varphi)i + \sin(\varphi)j + 0k$ as a rotation axis represented with series of $\varphi \in [0, \pi]$, from Rehman and Mandic (2010)

one corresponding to one 3D rotation axis. So the projection of the input signal along multiple direction vectors can be calculated by rotating the input signal about a set of vectors $\boldsymbol{q}$, rotation axes, which can also be presented by a set of unit quaternion, so $\boldsymbol{q} = 0 + \cos(\varphi)i + \sin(\varphi)j + 0k$, by φ an angle to the x-axis, see Fig. 2c.

So the trivariate input signal $x(t)$ can be considered as a pure quaternion signal and its projection is obtained by $P_{\theta_k}^{\varphi_n}(t) = e^{q\theta}x(t)\left(e^{q\theta}\right)^* \cdot \vec{k}$, where $\theta_k = k\pi/K$ for $k = 1, \ldots, K$, and $\varphi_n = n\pi/N$, for $n = 1, \ldots, N$. Afterwards the extrema envelope curves $e_{\theta_k}^{\varphi_n}(t)$ are obtained using a component-wise spline interpolation of the maxima of $P_{\theta_k}^{\varphi_n}(t)$ for all values of k and n. Finally, the mean of all the envelope curves is computed by $m(t) = \frac{1}{KN}\sum_{k=1}^{K}\sum_{n=1}^{N} e_{\theta_k}^{\varphi_n}$. The rest of the procedure is like the standard EMD. For illustration purpose, the results of the decomposition of a signal that comes from hand movement are displayed in Fig. 3.

To process multivariate signal, Rehman and Mandic (2009) introduced multivariate EMD (MEMD). It is the generalization of bivariate EMD and trivariate EMD. In this method, the input signal is projected along different directions in n-dimensional spaces. Then the extrema of such projected signals are interpolated component-wise to generate multiple n-dimensional envelopes. Then such envelopes are averaged to obtain the local mean.

To represent direction vectors in an n-dimensional space in the Euclidean coordinate system, the points on the surface of corresponding unit $(n-1)$ spheres are considered, indeed each point on the sphere surface corresponds to one direction vector from the center of the sphere.

The accuracy of the estimate envelopes is coupled to how uniformly these points, i.e., the multiple direction vectors, are selected. They can be obtained by uniform sampling based on a low-discrepancy Hammersley sequence as suggested by Rehman and Mandic (2009). For visualization purposes in the case of a trivariate signal, this sampling is illustrated in Fig. 4a.

The uniformly sampled direction vectors in multi-dimensional spaces, i.e., fixed distribution of direction vectors, are quite suitable for circular data with equal channel (component) powers. However, in the real world, there is a power discrepancy and/or inherent correlation between data channels so the density of projections should match the signal dynamics. To overcome this problem nonuniformly sampled bivariate EMD (NS-BEMD); (Ahrabian et al. 2013) and nonuniformly sampled trivariate EMD (NS-TEMD); (Hemakom et al. 2015) were proposed to process bivariate

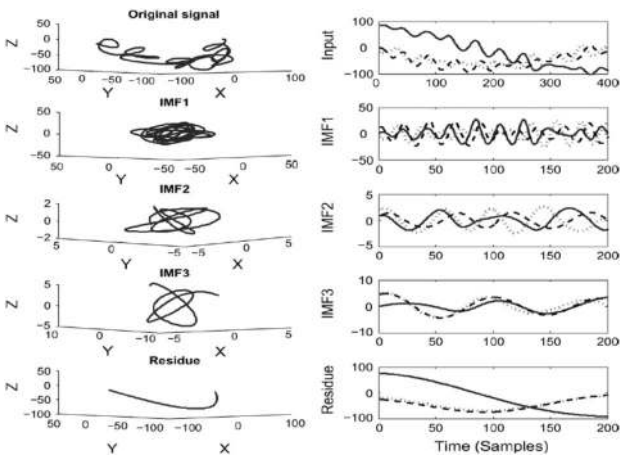

Fig. 3 Decomposition of a hand movement signal by trivariate EMD, from Rehman and Mandic (2010)

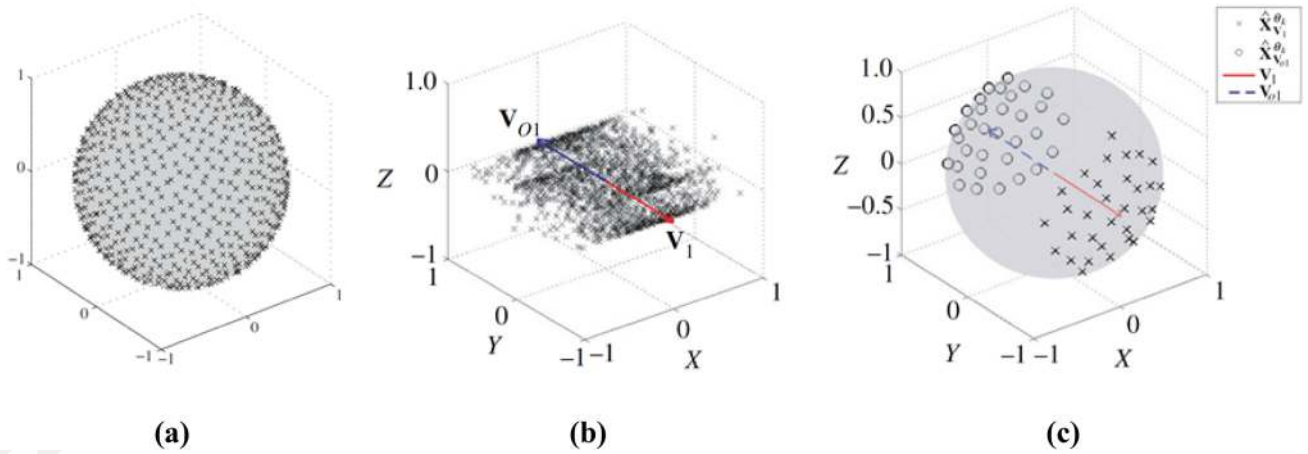

Fig. 4 **a** Direction vectors for taking projections of a trivariate sig-nal on a two-sphere generated by a low-discrepancy Hammersley sequence, from Rehman and Mandic (2009); **b** scatter plot of the trivariate data, first principal components and its diametrically opposite vector; **c** projected vectors adapted to $\alpha = 1$, from Hemakom et al. (2016)

and trivariate signals, respectively. In both methods, the directions of principal importance and the interchannel power imbalance are used to map the uniformly sampled direction set to non-uniform sampling, i.e., elliptically distributed points along the directions of principal importance. NS-TEMD uses all the eigenvectors and eigenvalues of the trivariate signal covariance matrix to determine the directions and interchannel imbalance. Applying the same method in the case of a multivariate signal is questionable since the direction of global highest curvature of the original input signal may not always align with the direction of the local first principal component of each sifting input, resulting in a suboptimal estimate of the local mean.

To overcome this shortcoming, a new approach called adaptive-projection intrinsically transformed MEMD (APIT-MEMD) was introduced by Hemakom et al. (2016). The direction of the first principal component that reflects the largest power imbalance and/or correlation in the channels of the multivariate signal is determined adaptively. Indeed, in each sifting process, the vectors that are used to relocate uniform pre-generated direction vectors are defined locally.

Consider an n-variate signal $\{s(t)\}_{t=1}^{\mathrm{T}} = \{s_1(t), s_2(t), \ldots, s_n(t),\}$ as an input for each sifting process; in APIT-MEMD, the procedure of computing adaptive direction vectors is as follows:

1. Determine the first principal component of $\boldsymbol{s}(t)$;
   perform the eigenvalue decomposition of the covariance matrix given by, $C = \mathrm{E}\{\boldsymbol{s}\boldsymbol{s}^T\} = \mathbf{V}\boldsymbol{\Lambda}\mathbf{V}^{\mathrm{T}}$ (with $\mathrm{E}\{.\}$ the statistical expectation operator and $(.)^{\mathrm{T}}$ the transpose operator), where $\mathbf{V} = [\mathbf{v}_1, \mathbf{v}_2, \ldots, \mathbf{v}_n]$ is the eigenvector matrix and $\boldsymbol{\Lambda} = \mathrm{diag}\{\boldsymbol{\lambda}_1, \boldsymbol{\lambda}_2, \ldots, \boldsymbol{\lambda}_n\}$ is the eigenvalue matrix, with $\boldsymbol{\lambda}_1$ the largest eigenvalue corresponding to eigenvector $\mathbf{v}_1$ i.e., the first principal component.
2. Construct a vector pointing in the diametrically opposite direction to the first principal component vector in n -dimensional space; $\mathbf{v}_{01} = -\mathbf{v}_1$.
3. Uniformly sample an $(n-1)$ sphere using the Hammersley sequence to generate a set of K-direction vectors $\{x^{\theta_k}\}_{k=1}^{K}$.
4. Compute the Euclidean distances from each of the uniform direction vectors to $\mathbf{v}_1$.
5. Relocating of uniform direction vectors as follows: half of all the uniform projection vectors, $x_{\mathrm{v}_1}^{\theta_k}$, nearest to $\mathbf{v}_1$, are relocated using $\hat{x}_{v_1}^{\theta_k} = \frac{x_{v_1}^{\theta_k} + \alpha \mathbf{v}_1}{\left| x_{v_1}^{\theta_k} + \alpha \mathbf{v}_1 \right|}$, where $0 \le \alpha \le 1$ controls the densities of the projection vectors around the first principal component. The other half of all uniform projection vectors, $x_{\mathrm{v}_{01}}^{\theta_k}$, nearest to $\mathbf{v}_{01}$, are relocated using $\hat{x}_{v_{01}}^{\theta_k} = \frac{x_{v_{01}}^{\theta_k} + \alpha \mathbf{v}_{01}}{\left| x_{v_{01}}^{\theta_k} + \alpha \mathbf{v}_{01} \right|}$.

The α value reflects the degree of power imbalances across the data channels: when $\alpha = 0$, it means that no power imbalance exists or is not taken into account in the decomposition. By increasing α the direction vectors will be more clustered around the first principal component of the multivariate signal as shown in Fig. 4b, c for $\alpha = 1$.

Once the adaptive direction vectors $\hat{x}_{\mathrm{v}_1}^{\theta_k}$ and $\hat{x}_{\mathrm{v}_{01}}^{\theta_k}$ have been obtained, they are used in the MEMD algorithm to decompose the multivariate signal, according to the following steps:

1. Compute a projection, denoted by $\left\{P^{\theta_K}(t)\right\}_{t=1}^{\mathrm{T}}$ of the input signal $\{s(t)\}_{t=1}^{\mathrm{T}}$ along the direction vectors $\hat{x}_{\mathrm{v}_1}^{\theta_k}$ and $\hat{x}_{\mathrm{v}_{01}}^{\theta_k}$, for $k = 1, \ldots, K$ (the whole set of direction vectors), giving $\left\{P^{\theta_K}(t)\right\}_{k=1}^{K}$ as the set of projections.
2. Find the time instants $\left\{t_i^{\theta_k}\right\}$ corresponding to the maxima of the set of projected signals $\left\{P^{\theta_K}(t)\right\}_{k=1}^{K}$.

Interpolate component-wise $\left[t_i^{\theta_k}, \boldsymbol{s}\left(t_i^{\theta_k}\right)\right]$, via cubic spline interpolation, for all values of k to obtain multivariate envelope curves $\left\{e^{\theta_K}(t)\right\}_{k=1}^{K}$.

3. For a set of K direction vectors, calculate the mean of the envelope curves as
   $\mathbf{m}(t) = \frac{1}{K}\sum_{k=1}^{K} e^{\theta_k}(t)$.
4. Extract the detail $\mathbf{h}(t) = \boldsymbol{s}(t) - \mathbf{m}(t)$, if $\mathbf{h}(t)$ fulfills the stoppage criterion for multivariate IMF (see below), it is considered as an IMF and then re-apply the above procedure to $\mathbf{s}(t) - \mathbf{h}(t)$, otherwise re-apply it to $\mathbf{h}(t)$.

The stoppage criteria used for standard EMD can also be adopted for MEMD and APIT-MEMD. However, since the extrema cannot be properly defined for multivariate signals, the condition for equality of the number of extrema and zero crossings is not imposed. It should be emphasized that for the multivariate IMF, the sifting process can be stopped when all the projected signals fulfill the stoppage criterion. In MEMD as a rule of thumb, the number of projections should be at least five to six times more than the number of data channels to generate meaningful IMFs. Nevertheless, when using APIT-MEMD, fewer direction vectors are required since they are more clustered around the first principal component.

The standard EMD suffers from the mode (scale)-mixing problem, i.e., a single mode consisting either of signals of widely disparate scales (oscillations) or a single scale appearing in different modes (mode splitting). Mode-mixing can often occur when the process contains intermittent high-frequency oscillations and/or variation of instantaneous amplitude and frequency of the modes.

To overcome this defect, the ensemble empirical mode decomposition (EEMD) was proposed by Wu and Huang (2009). It defines the IMF components as the mean value of an ensemble trial. In each trial, a random white noise of finite amplitude is added to the signal, then the standard EMD is applied on the polluted signal resulting in series of IMF components. Obtaining the (ensemble) mean of corresponding IMFs of the different decompositions leads to the final result. A collection of white noise neutralizes itself in a time/space ensemble mean of enough trials; therefore, only the desired signal can persist in the final mean result.

The addition of white noise provides a uniformly distributed scale in time–frequency space. The intrinsic oscillations in the signal with different scales would automatically project onto similar reference scales established by the white noise. Therefore, the intrinsic local oscillation can be filtered adaptively to proper scales via the natural filter bank of EMD associated with the added white noise as introduced by Flandrin et al. (2004) and Wu and Huang (2004). The input noise level ε_0 depends on the target signal-to-noise ratio (SNR), in practice $0.1 < \varepsilon_0 < 0.4$, it should be noted that while the data are dominated by high-frequency signals, the amplitude of noise must be set to a small value and vice versa (Wu and Huang 2009). The number of the ensemble trials NE should be of the order of 100 as specified in Wang et al. (2014).

Similar to the standard EMD, multivariate extensions of EMD using the noise-assisted mode can be considered to alleviate the mode-mixing problem (Rehman and Mandic 2011; Rehman et al. 2013). The added white noise channels occupy a broad range in the frequency spectrum. The decomposition aligns its different components (IMFs) in accordance with the quasi-dyadic[1] filter bank structure, with each IMF containing a separate scale of the input signal. By doing this, the IMFs of the original signal also align themselves in accordance with the structure of a quasi-dyadic filter bank.

In noise-assisted MEMD (NA-MEMD) unlike EEMD, the White Gaussian Noise (WGN) is not directly added to the channels of the multivariate signal, but is considered as an adjacent subspace. The composite signal is processed by MEMD or APIT-MEMD and then the resulting IMF channels corresponding to white noise are discarded thus leading to a set of IMFs associated with only original input. The noise powers should be close to those of the input signal channels, such that the WGN processes themselves do not cause a power imbalance. One can choose the noise power as a mean of input signal channel powers. The powers in each of the noise channels are identical and the total perturbation is a linear mixture of the noise channels.

A single realization of l-channel WGN in the decomposition of a multivariate signal may lead to slightly different outputs for different trials of l-channel WGN. Therefore, the uniqueness of the decomposition is questionable. To overcome this shortcoming, an ensemble approach inspired by EEMD was adopted by Rehman et al. (2013), called ensemble-NA-MEMD, whereby an input multivariate signal was decomposed several times (order of 100) by MEMD, each time by a different set of l-channel noise. Then the set of

[1] The dyadic filter bank decomposes a broad band signal into a collection of successively band-limited components by repeatedly dividing the frequency range.

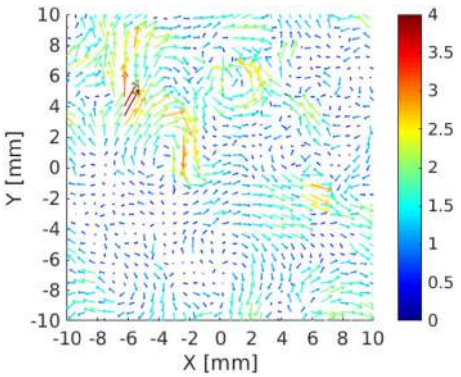

Fig. 5 Original data; an instantaneous velocity field obtained experi-mentally in homogeneous and isotropic turbulence condition

multivariate IMFs obtained from MEMD is ensemble averaged to obtain the output.

3 Bivariate 2D-EMD

The potential of bivariate EMD (BEMD) to fuse two images, i.e., data multiscale fusion, was already investigated (Looney and Mandic 2009; Rehman et al. 2009). Different studies reported a significantly better performance of MEMD-based fusion schemes compared with those based on discrete wavelet transform (DWT) or principal components analysis (PCA) (Mandic et al. 2013; Rehman et al. 2015). In fact, by insightful viewpoint, these results reveal the ability of the EMD approach to relate multiple components (IMFs) of a multichannel signal whose components are located in two-dimensional space.

Knowing about these potential of MEEMD, in this study, we propose to use Ensemble NA-APIT-MEMD to process a two-dimensional velocity field. The instantaneous 2D velocity field is considered as a 2D bivariate signal $\mathbf{U}(x, y) = U(x, y) + V(x, y)$, where U and V are the velocity components in x- and y-directions, respectively. The algorithm of decomposition is the same as for multi-dimensional ensemble empirical mode decomposition (MEEMD) that was introduced by Wu et al. (2009) for decomposition of mono-variate multi-dimensional signal. First, ensemble NA-APIT-MEMD is applied to each row (or column) of the bivariate 2D signal, i.e., decomposition along one dimension.

Afterwards, it is applied to each column (or row) of the results of the decompositions in the first step, i.e., decomposition along the second dimension. The final components are obtained by applying the comparable minimal scale principle, i.e., "among all the components resulted from applying EEMD in two orthogonal directions, the combination of the components having comparable minimal scales would give the most meaningful results" (Wu et al. 2009).

To illustrate this 2D decomposition method, an instantaneous experimental HIT velocity field (Galmiche et al. 2014) is presented in Fig. 5. It is considered as $f(m, n)$ gridded spatially as 127×127 two-dimensional data. This field is decomposed by the above procedure; the horizontal direction components obtained by application of ensemble NA-APIT-MEMD on each row of this velocity field are illustrated in Fig. 6. It should be mentioned for the demonstration purpose and to avoid redundancy, only the results of U component velocity are presented.

Each of these 2D components is decomposed in the vertical direction with their results illustrated in the vertical columns in Fig. 7. Hence, the original two-dimensional data are represented by

$$f(m, n) = \sum_{k=1}^{K} \sum_{j=1}^{J} h_{j,k}(m, n),$$

where $h_{j,k}$ denotes the two-dimensional component that is located in the jth row and kth column (Fig. 7), here $J = K = 6$. It should be point out that the number of modes in each direction is at most $o\left(\log_2 N\right)$, where N is the signal length.

Figure 7 reveals some oriented scales of the original data and also some similar characteristics in different components can be observed. The components of each row have approximately the same vertical scale and the components of each column have approximately the same horizontal scale. Also the horizontal (vertical) scales of each row (column) increase as k (j) increases. Another important property of

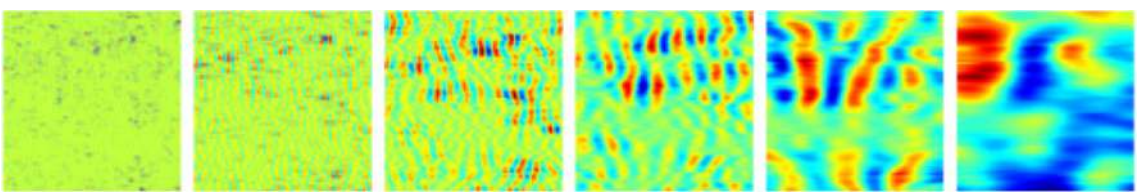

Fig. 6 The horizontal direction components for the U velocity component, left to right from high to low spatial frequency, the scale in each panel is different and blue color corresponds to negative values

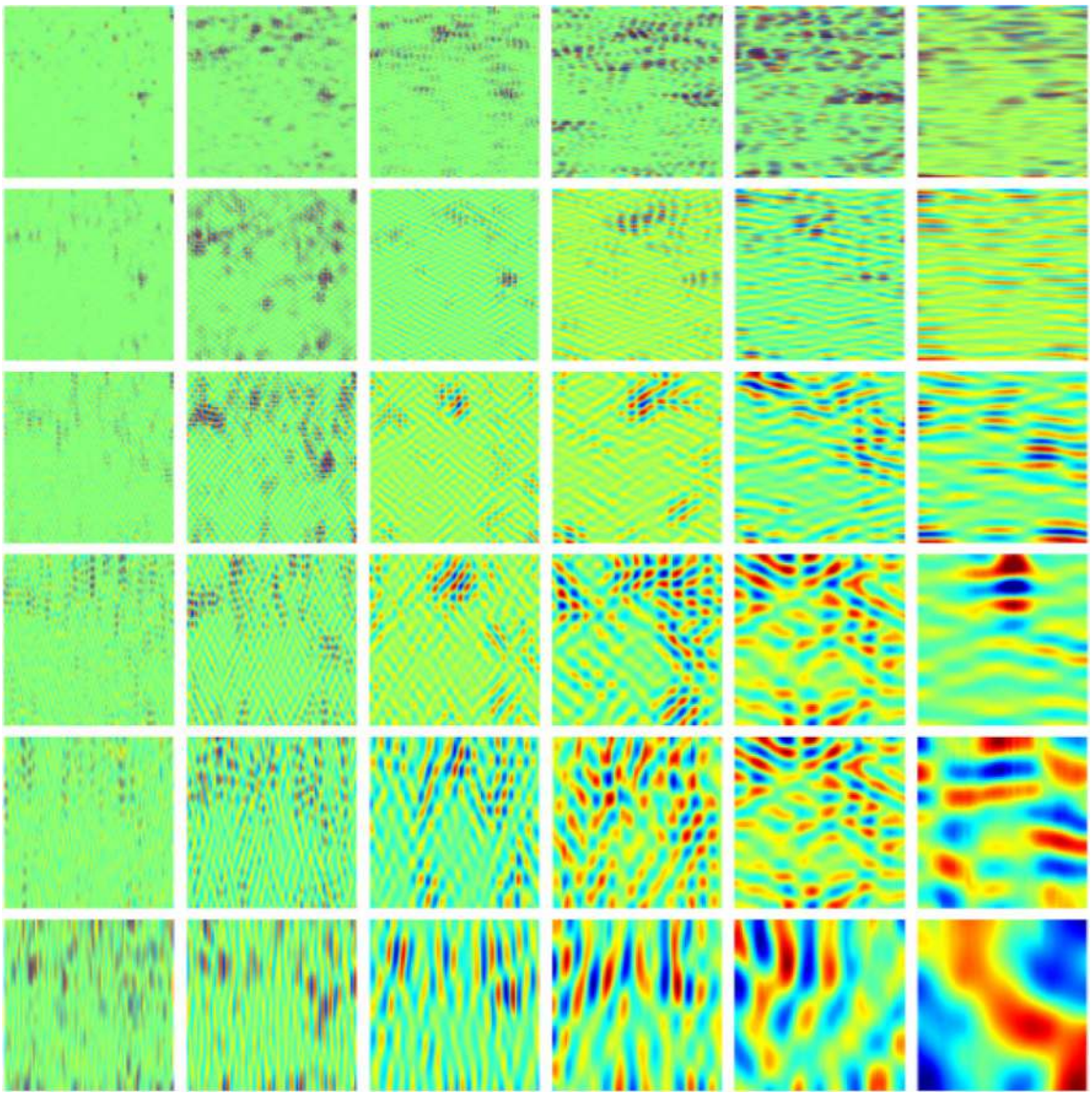

Fig. 7 The components associated with U velocity components resulting from applying Ensemble NA-APIT-MEMD in two orthogonal direc-tions on the original data (Fig5), the scale in each panel is different and blue color corresponds to negative values

the components displayed in Fig. 7 is that they have approximately the same minimal scale for the first row components $h_{1,k}$ in the vertical direction and for the first column components $h_{j,1}$ in the horizontal direction as shown in Fig. 8.

So using the comparable minimal scale principle the final ith 2D bivariate IMFs can be obtained by $\mathrm{BIMF}_i = \sum_{k=i}^{K} h_{i,k} + \sum_{j=i+1}^{J} h_{j,i}$. The scheme of this combination strategy is presented in Fig. 9a, where the neighbor components with the same shade are summed to construct a final mode. The horizontal components of the final bivariate modes of the original velocity field (Fig. 5) are presented in Fig. 9. It should be mentioned that the decomposition is independent of the selection of the orthogonal reference frame so the results are not sensitive to the choice of direction (first horizontal and then vertical or vice versa) for applying ensemble NA-APIT-MEMD.

By this way, the two components of the velocity field, horizontal U and vertical V velocities are decomposed simultaneously. The major advantage of such an analysis is that the inter-correlation between the two components of the velocity during the decomposition is considered hence a set of common scales can be find between the same-index IMF of each component; in addition, the number of IMFs for each

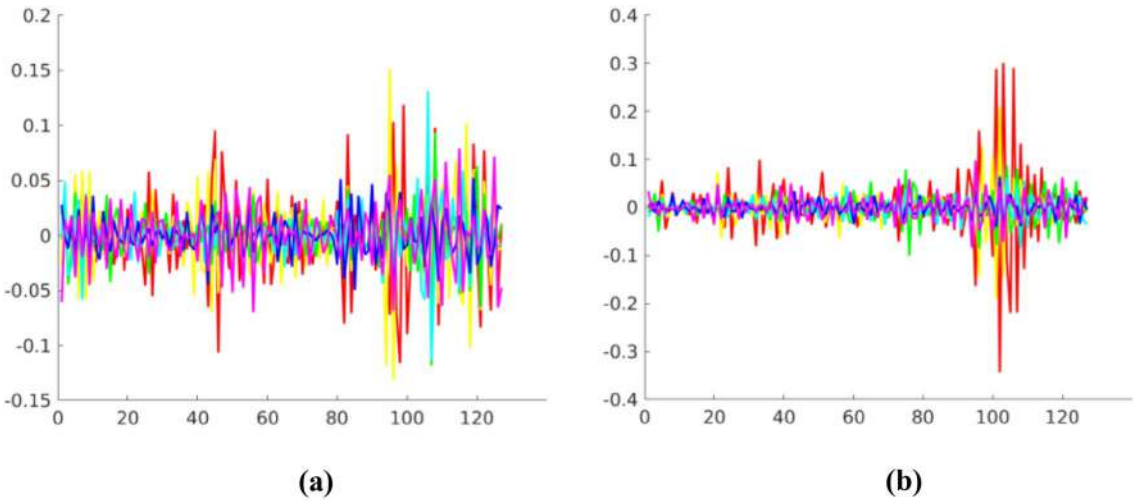

Fig. 8 **a** Horizontal velocity oscillation along the central column (the 63rd column) in the vertical direction for $h_{1,k}$ components; **b** horizontal velocity oscillation along the central row (the 63rd row) in the horizontal direction for $h_{j,1}$ components. In each figure the different colors correspond to different components: red lines; j or $k = 1$, yellow lines; j or $k = 2$, green lines; j or $k = 3$, light blue lines; j or $k = 4$, blue lines; j or $k = 6$, magenta lines; j or $k = 6$

components is the same that leads to have the physically meaningful modes.

The final results of the decomposition of this HIT velocity field by the proposed bivariate 2D-EMD are presented in Fig. 10, the two components U (left column) and V (right column) and their different IMFs are plotted row by row.

For bivariate 2D-EMD analysis, two adjacent WGN channels were used. The influence of the number of noise channels on the decomposition requires a detailed investigation which is beyond the scope of this study. However, it should be pointed out that having a noise channel would enforce the dyadic filter bank property and also that increasing the number of noise realizations would further reduce the degree of overlap (mode-mixing) between the IMFs. In this study, the simulations suggest that the choice of the two WGN can lead to the satisfactory results and the use of more WGN has no significant influence on the resulting IMFs.

To not modify the degree of power imbalance between data channels, the noise variance is equal to the mean variance of the two principal input signals, i.e., U and V velocity components.

The number of direction vectors in MEMD and APIT-MEMD varied from 32 to 256 (from moderat to very high), indeed it should be considerably greater than the dimensionality of the signal to extract meaningful IMFs (Rehman and Mandic 2009). In this study to compute the mean envelope, the input multi-component signal is projected in 64 directions, actually no change is observed in our results by increasing this value.

The projection density α was set to 0.3 due to low power imbalance between U and V velocity components. The number of ensemble realizations NE is set to 100, it is the same as EEMD when processes mono-variate signals (Wang et al. 2014) and for the sifting process, the mean-value stoppage criterion with (0.05, 0.5, 0.05) is used. Note that the projection density and stopping criterion parameters used in this investigation are standard values widely employed in EMD analysis. It is worth noticing that the mono-dimensional APIT-MEMD algorithm was provided by Hemakom et al. (2016) and Rehman and Mandic (2010), it is available in https://www.commsp.ee.ic.ac.uk/~mandic/research/emd.htm.

As one can see in Fig. 10, different components of the input velocity field are matched in mode number and the first mode of each component U and V contains the highest order of fluctuations as it is associated with the smallest scale of the velocity field. When the decomposition progresses, the spatial frequency of the fluctuations in the modes decrease and the last mode of each component represents the tendency of the input signal associated with the large-scale structure of the velocity field. This property of bivariate 2D-EMD decomposition can be verified by computing the spatial power spectral density of each component U and V of bivariate IMFs, presented in Fig. 11. It is observed that the same-index modes across data channels contain common scales and their frequency bands overlap, i.e., scale alignment. In addition, the energy of different modes is concentrated in different wavenumbers

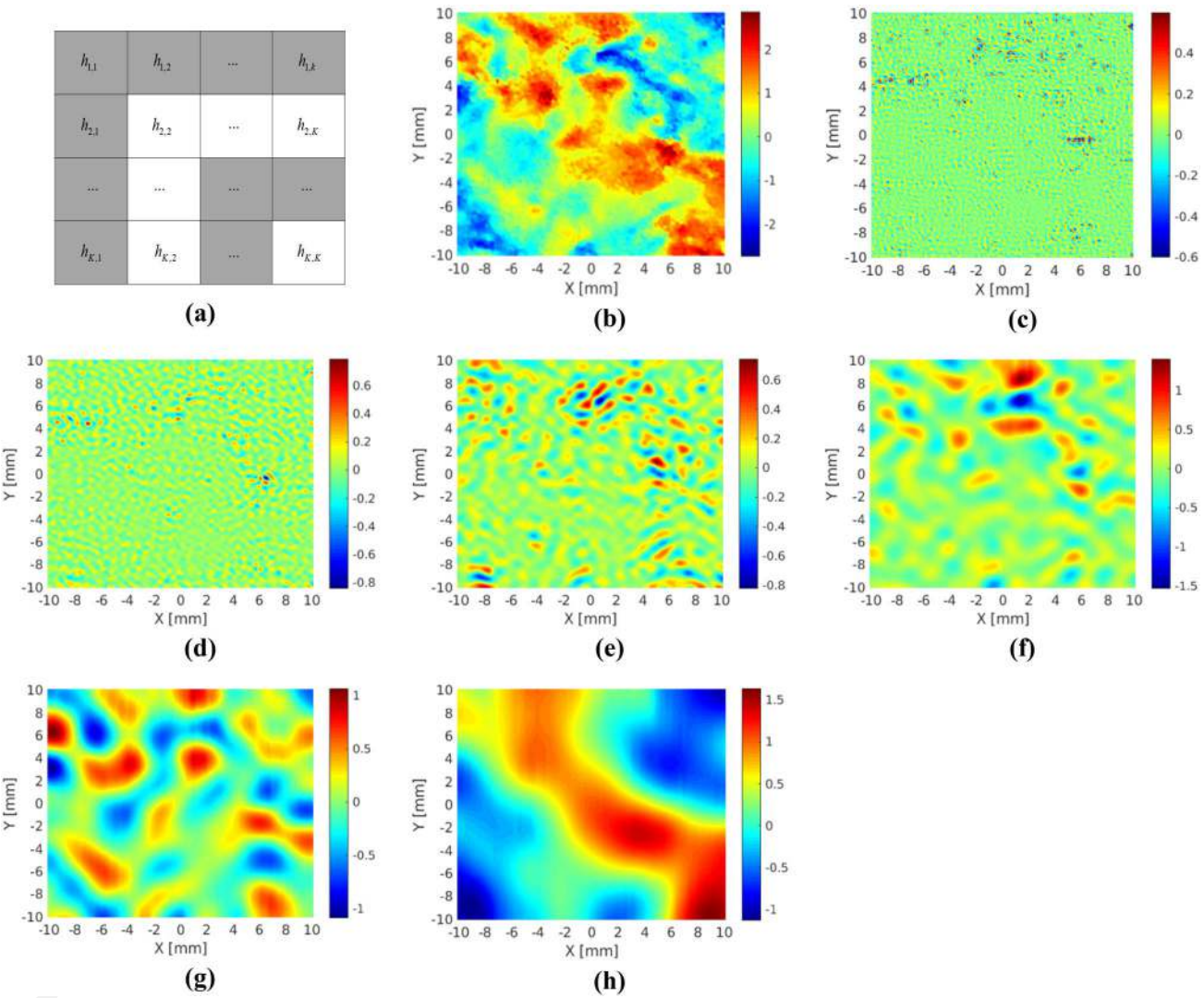

Fig. 9 a Combination strategy for different components resulting from applying ensemble NA-APIT-MEMD in two orthogonal directions; b horizontal velocity component U of the original velocity filed displayed in Fig. 5 and the horizontal components of the final bivari-ate modes: c–h mode (1, 2, 3, 4, 5 and 6, respectively), the unit is ms^{-1}

(scales), confirming the very low degree of mode-mixing in the decomposition.

It should be pointed out that since the modes are not orthogonal with respect to one another, the sum of their energy spectrum, that is associated with two velocity components, does not superimpose on the input instantaneous velocity spectra, as presented in Fig. 11 by gray and black lines, respectively.

As noticed in computation of the power spectrum only the fluctuations of the instantaneous velocity are taken into account and the spatial mean of the velocity is subtracted. Also the power spectral density is computed using Welch's method with the length 127 (size of velocity field) of the FFT with 50% overlapping segments and Hann window function.

4 Validation of bivariate 2D-EMD

To assess the ability of the proposed bivariate 2D-EMD in the decomposition of a turbulent velocity field to separate large-scale organized motions from the HIT flow field, the following methodology was designed and tested. An experimental homogeneous and isotropic turbulent (HIT) flow was used as an initial velocity signal, $\mathbf{U}_i(x, y)$ including U and V components in x- and y-directions,

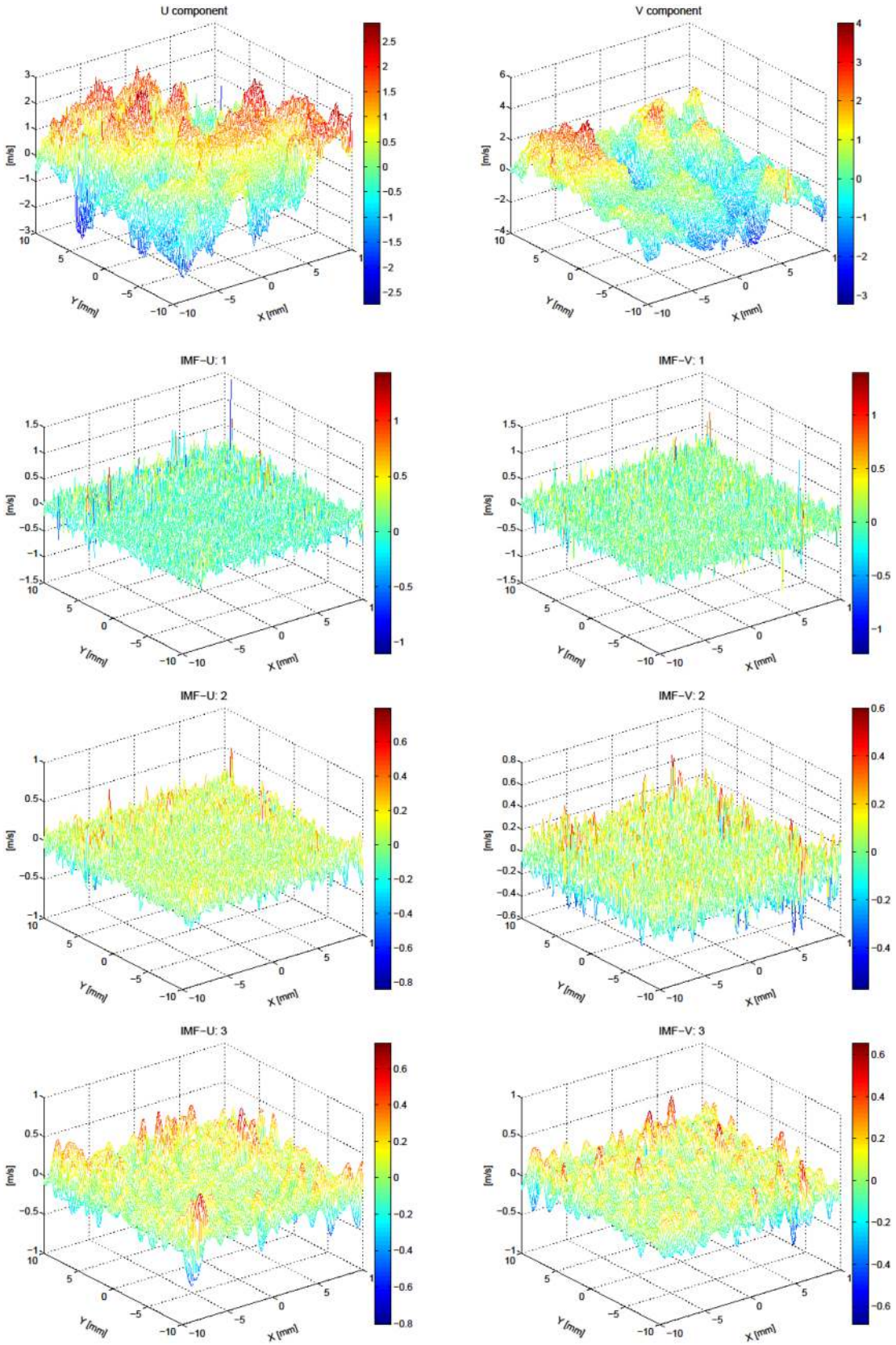

Fig. 10 Horizontal and vertical components of instantaneous velocity field, presented in Fig. 5, in the first panel and the different modes resulting from bivariate 2D-EMD analysis

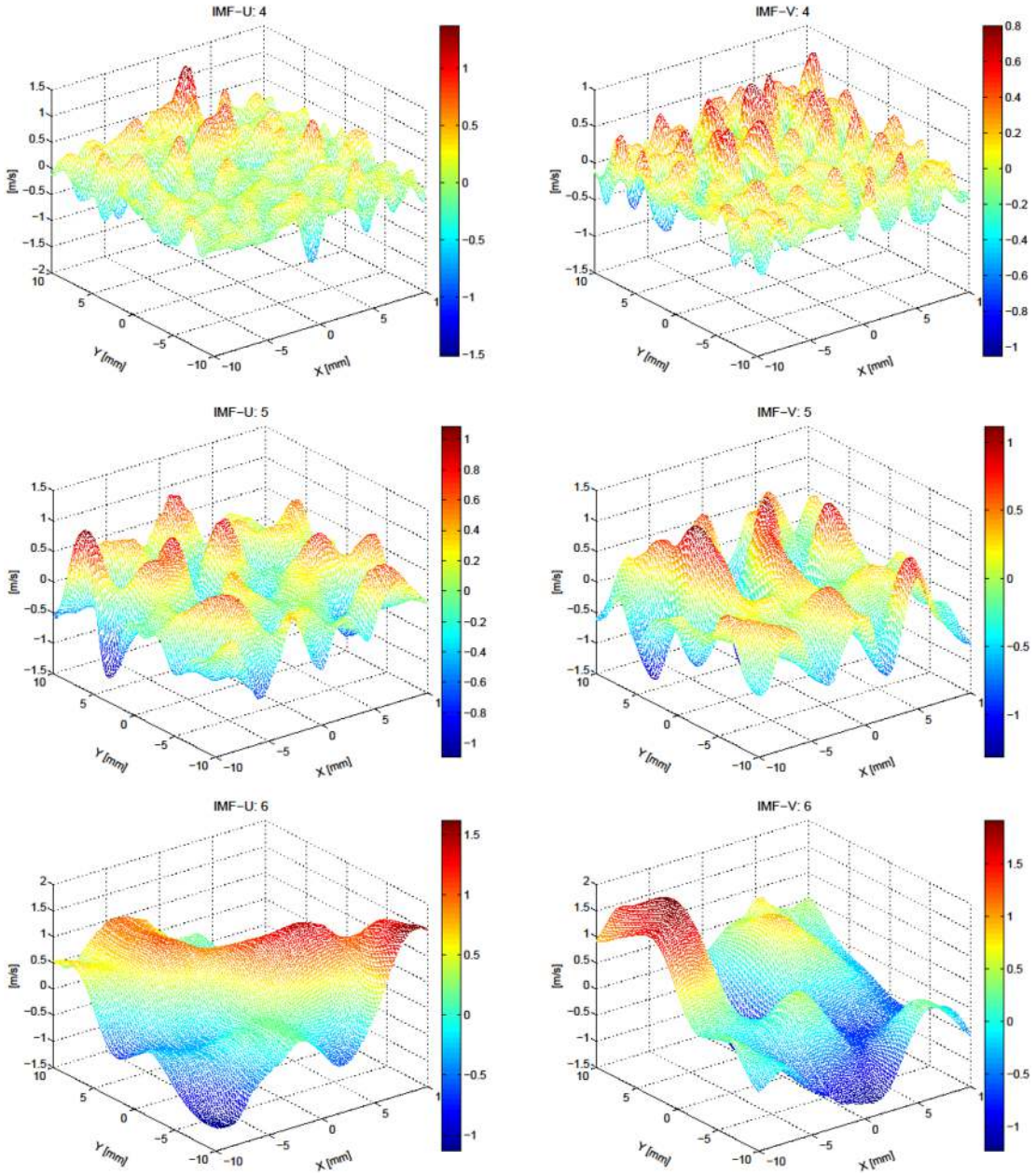

Fig. 10 (continued)

respectively. This flow was generated inside a spherical combustion chamber with the help of six fans. Velocity fields of 127×127 vectors were obtained by means of High Speed-PIV (2D2C) at 3.5 kHz frequency with a spatial resolution of 0.16 mm corresponding to a field of view of $20.32 \times 20.32\,\text{mm}^2$. Galmiche et al. (2014) previously characterized this homogeneous and isotropic turbulent flow field in terms of integral length and temporal scales and energy spectra.

For the purpose of the present study, the initial HIT velocity fields were perturbed by a synthetic Lamb–Oseen vortex $\mathbf{P}(x, y)$ to simulate a large-scale flow organized structure, such as Tumble motion in engine in-cylinder flows. The amplitude A, scale l and the position of the added vortex, called perturbation signal, were varied with respect to the initial HIT. The 2D perturbed velocity field $\mathbf{U}_p(x, y) = \mathbf{U}_i(x, y) + \mathbf{P}(x, y)$ was decomposed by bivariate 2D-EMD into different modes, i.e., IMFs. Based on an energy criterion the original, i.e., initial turbulence flow can be recovered within the modes and separated from perturbation.

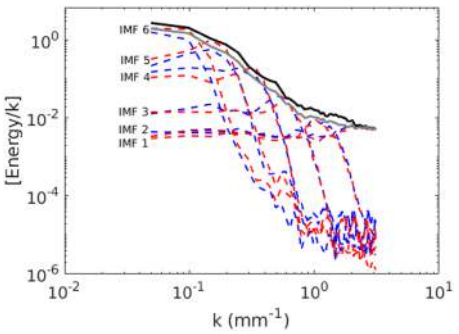

Fig. 11 Power spectra of each component of bivariate IMFs corre-sponding to component U (dashed red lines) and V (dashed blue lines) of the input velocity field. Power spectrum of instantaneous velocity (black line) and the sum of all bivariate spectra (gray line)

To evaluate the quality of separation, the energy spectrum of the original HIT flow and recovered turbulent velocity field was compared. Also the relative mean square error between the added synthetic vortex and the separated perturbation were computed.

To seek a demonstration, the procedure was applied to three instantaneous different velocity fields, called in the following HIT fields 1, 2 and 3. Some discrepancies can be seen, such as the different structures and the range of vector values, as shown in Fig. 12. In the following, only the perturbed and recovered velocity fields associated with field 1, taken as an example, will be presented.

4.1 Influence of the vortex amplitude

The amplitude A of the added vortex was varied from the input HIT turbulent kinetic energy value (TKE $\simeq 1\,\mathrm{m^2\,s^{-2}}$) as 10, 5, 2 and 1. The scale (size) of the synthetic vortex was set arbitrarily to five times the longitudinal integral scale of the HIT flow; $l = 5 \cdot L_{(Ux,Vy)}$ with $L_{(Ux,Vy)} = 3.2\,\mathrm{mm}$ and the center of the vortex was positioned at the center (0, 0) as shown in Fig. 13.

In Fig. 14a, b, the first initial HIT and the 2D perturbed velocity fields obtained from the addition of the vortex in Fig. 13a with $A = 10\,\mathrm{ms^{-1}}$ are presented, respectively. The perturbed velocity field is decomposed by bivariate 2D-EMD.

To recover the initial HIT velocity field within the different modes, the energy criterion related to the signal intensity is used. It is defined as $E_n = 0.5\left(\left\langle U_n^2\right\rangle + \left\langle V_n^2\right\rangle\right)$ with n index the mode number and the symbol "$\langle . \rangle$", the spatial average. So when applied to a 2D signal it leads to

$$E_n = \frac{0.5}{n_x.n_y}\sum_{i=1}^{n_x}\sum_{j=1}^{n_y}\left(U_n^2(x_i,y_i) + V_n^2(x_i,y_i)\right),$$

where n_x and n_y are the total number of points within the 2D signal in the x- and y-directions, respectively, here $n_x = n_y = 127$. The energy content computed for each mode is plotted in Fig. 15. As one can see, there is a sudden jump in the sixth mode. Therefore, the recovered velocity field that should ideally represent the initial HIT velocity field, i.e., high-frequency field, is defined as a sum of the first five modes (Fig. 14c), while the sixth mode is considered as the largest scale flow structure, i.e., low-frequency field (Fig. 14d). The same procedure was applied for HIT fields 2 and 3. The energy contents for both also present a strong jump from the 5th to the 6th modes.

The spatial power density spectra of the initial HIT, perturbed and recovered velocity fields for the three cases are presented in Fig. 16. The mean spatial power spectrum of the initial 8000 experimental instantaneous HIT flow fields is also depicted as an indicator. It can be observed that the spatial power spectral density from the recovered turbulent velocity field is always under this mean value for the lowest frequency number, i.e., the largest structures of the flow. Although it is well superimposed on the initial HIT flow in the inertial subrange, this feature is independent of the original HIT fields.

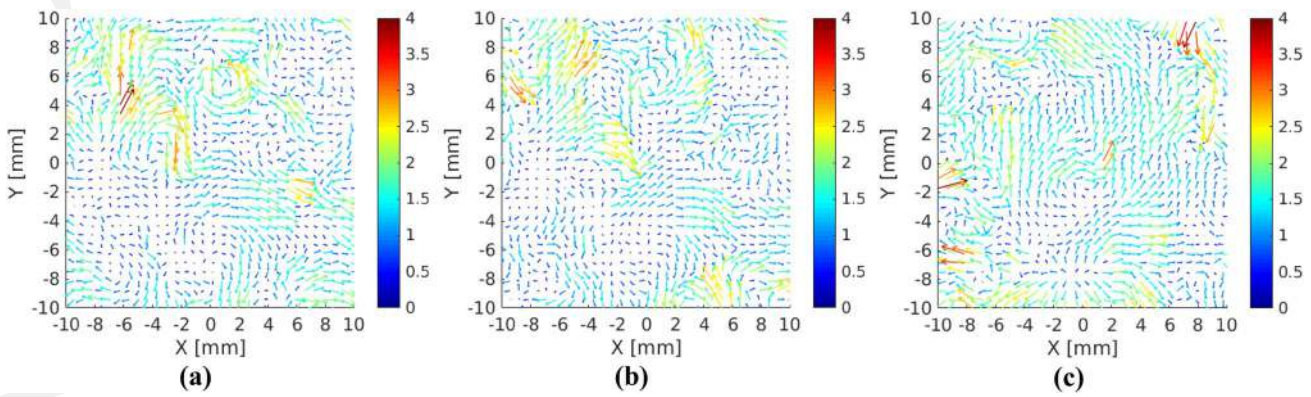

Fig. 12 Three experimental instantaneous HIT velocity fields, all four vectors are displayed. **a** HIT field 1; **b** HIT field 2; **c** HIT field 3

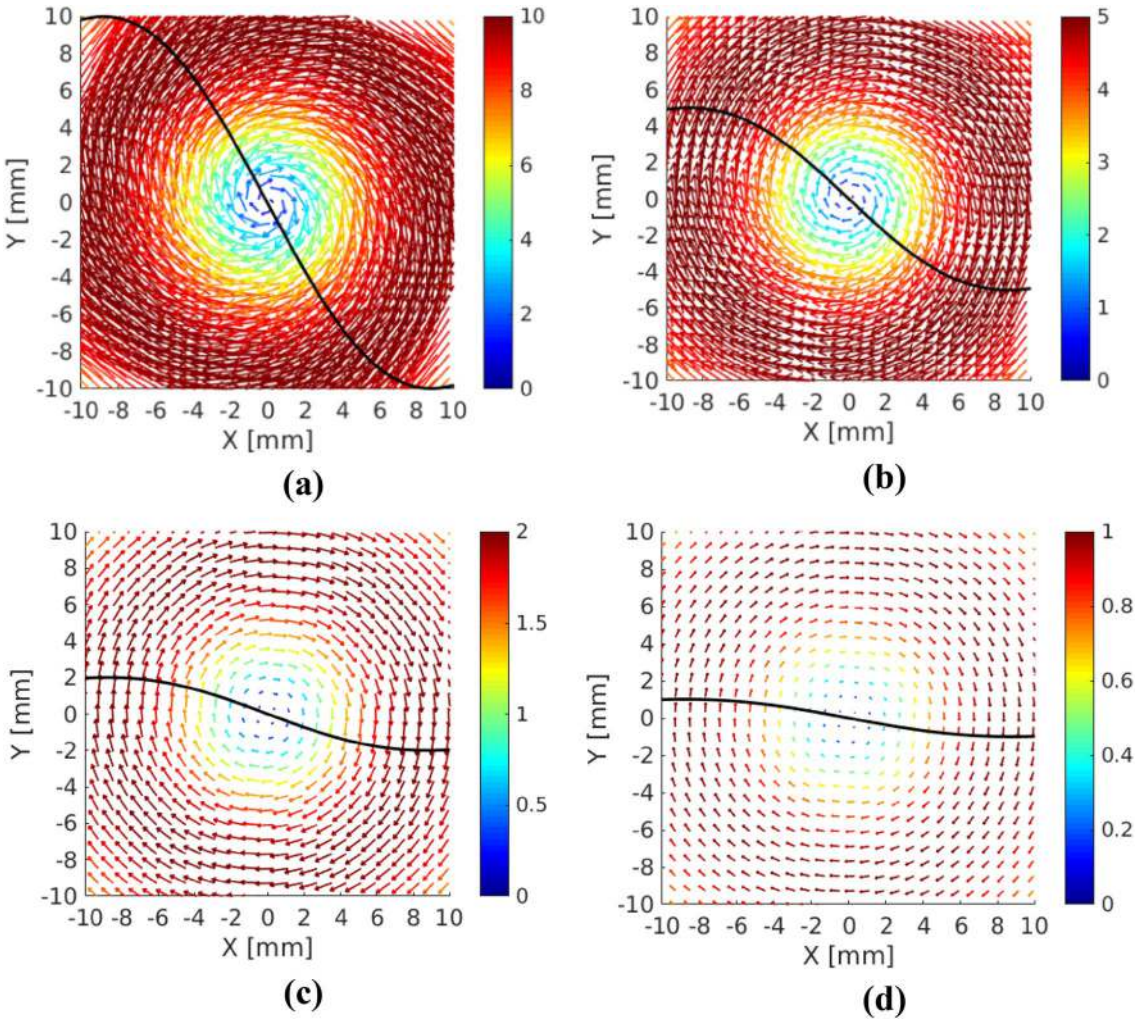

Fig. 13 Velocity field of the generated vortex centered in the middle, $l = 5 \cdot L_{(Ux,Vy)} = 16\,\text{mm}$ size for four different amplitudes. **a** $A = 10$; **b** $A = 5$; **c** $A = 2$; **d** $A = 1\,\text{ms}^{-1}$

The relative mean square error between the synthetic Lamb–Oseen vortex $\mathbf{P}(x, y)$ and separated flow low-frequency part $\mathbf{Lf}(x, y)$ can be computed to evaluate the relative accuracy of the results, as follows:

$$\sigma = \frac{\sum_{i=1}^{n_x} \sum_{j=1}^{n_y} |\mathbf{P}(x,y) - \mathbf{Lf}(x,y)|^2}{\sum_{i=1}^{n_x} \sum_{j=1}^{n_y} |\mathbf{P}(x,y)|^2},$$

where n_x and n_y are the total number of points in 2D velocity field in the x- and y-directions, respectively, here $n_x = n_y = 127$ and symbol "|.|" denotes the absolute value. Such an error in the case of $A = 10\,\text{ms}^{-1}$ is $\sigma = 0.6, 0.5$ and 1% for the three velocity fields. The results of this analysis for the perturbation amplitude of $A = 5$ and $2\,\text{ms}^{-1}$ are consistent with the previous case so they are not represented. In the case of $A = 5\,\text{ms}^{-1}$, the error is $\sigma = 2.3, 1.6, 3.1\%$ and for $A = 2\,\text{ms}^{-1}$, the error is $\sigma = 15.6, 9.7, 17.1\%$ for three velocity fields. For all velocity fields when the perturbation amplitude decreases, the value of σ becomes more important. This is mainly due to the small value, i.e., the low-velocity magnitude, in the dominator of σ equation that a small difference leads to the large error. For the case in which the perturbation amplitude is of the same order of magnitude as the TKE of the initial field, $A = 1\,\text{ms}^{-1}$, the analysis results for HIT Field 1 are displayed in Fig. 17.

The spatial power spectra of the initial HIT, perturbed and recovered velocity fields for the three under-study HIT fields are presented in Fig. 18. Although by observation the perturbation amplitude has a strong impact on the velocity–low-frequency part, Fig. 17d, the power spectra of the recovered velocity fields are superimposed on those of the initial HIT flows in the inertial subrange and the smallest scales.

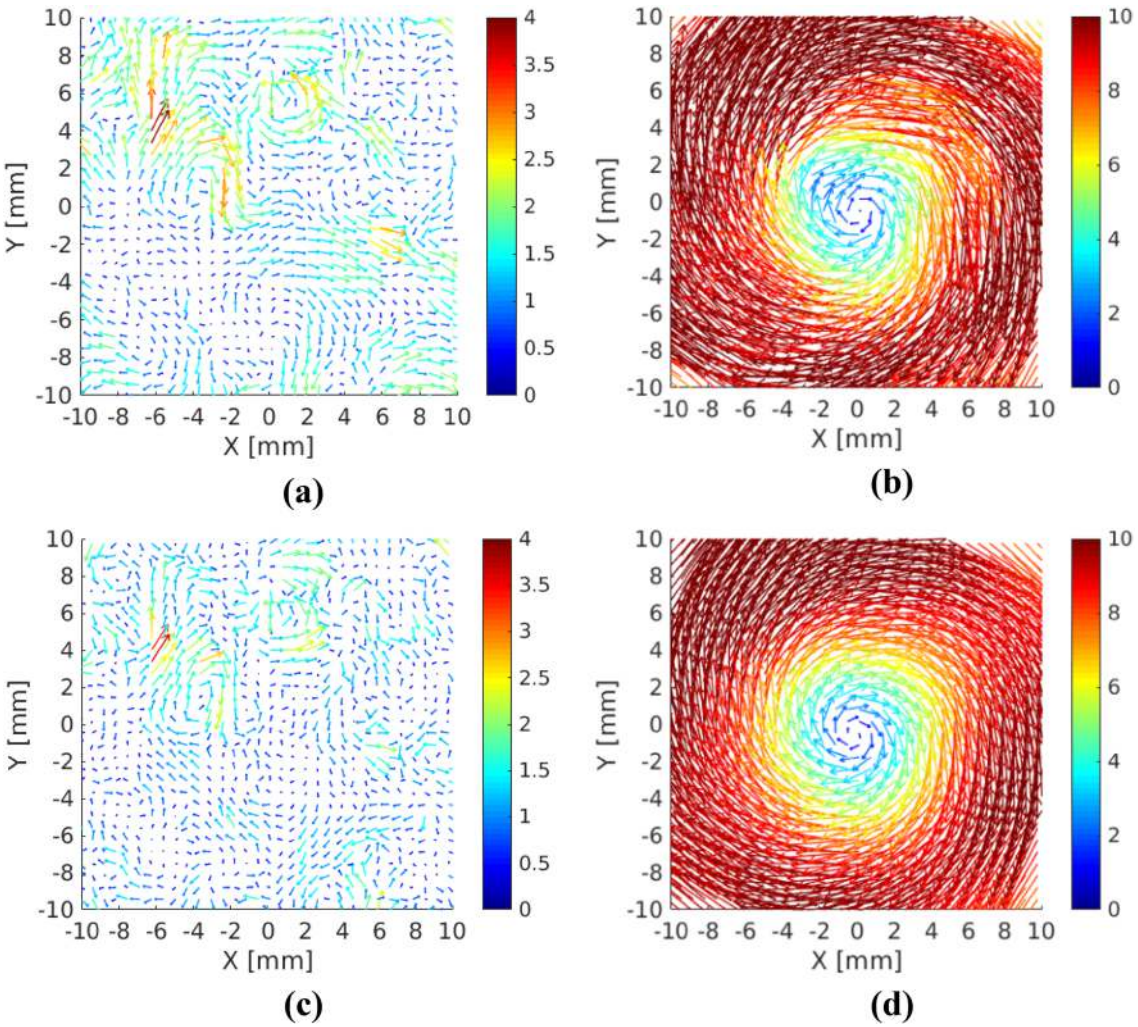

Fig. 14 Vortex amplitude $A = 10\ \mathrm{ms}^{-1}$, **a** initial HIT field 1; **b** perturbed velocity field; **c** recovered velocity field; **d** low frequency part

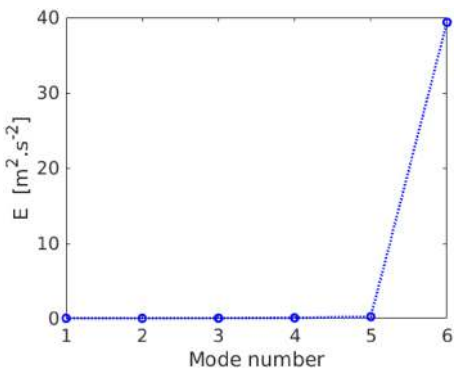

Fig. 15 Energy contents as a function of mode number

4.2 Influence of the vortex location

The location of the vortex center was varied relative to the initial HIT velocity field center to assess whether the bivariate 2D-EMD suffers from end-effect problems, i.e., decomposition of the 2D signal at the velocity field boundary. The vortex amplitude was set to $5\ \mathrm{ms}^{-1}$ and the scale $l = 16$ mm. To compare with the case of the centered vortex, two other cases were investigated: one with a vortex center located at mid-distance between the center and corner (top right) of the initial HIT field, and another with a center at the corner of the initial HIT field, as plotted in Fig. 19a, b, respectively.

These vortices were added as perturbation to the three HIT fields. An example of perturbed flow fields is given in Fig. 19c, d for HIT field 1. In Fig. 20, the spatial power spectra of the initial HIT, perturbed and recovered velocity fields are presented for both vortex locations and applied to the three HIT fields. The conclusion is the same as above: all the power spectra are superimposed on the initial HIT flow fields in the inertial subrange and the smallest scales, but in the region associated with large-scale structures, the energy

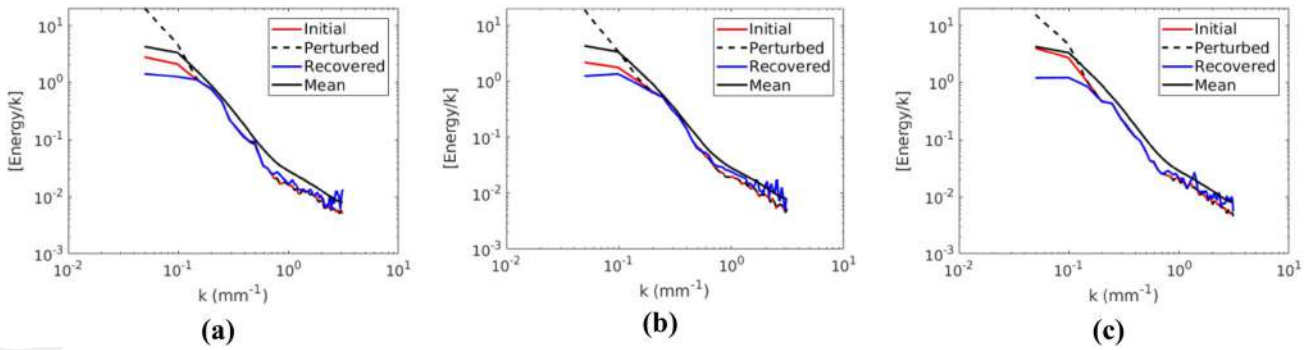

Fig. 16 $A = 10\,\mathrm{ms}^{-1}$, spatial power spectra of the initial HIT, perturbed and recovered velocity fields **a** HIT field 1; **b** HIT field 2; **c** HIT field 3

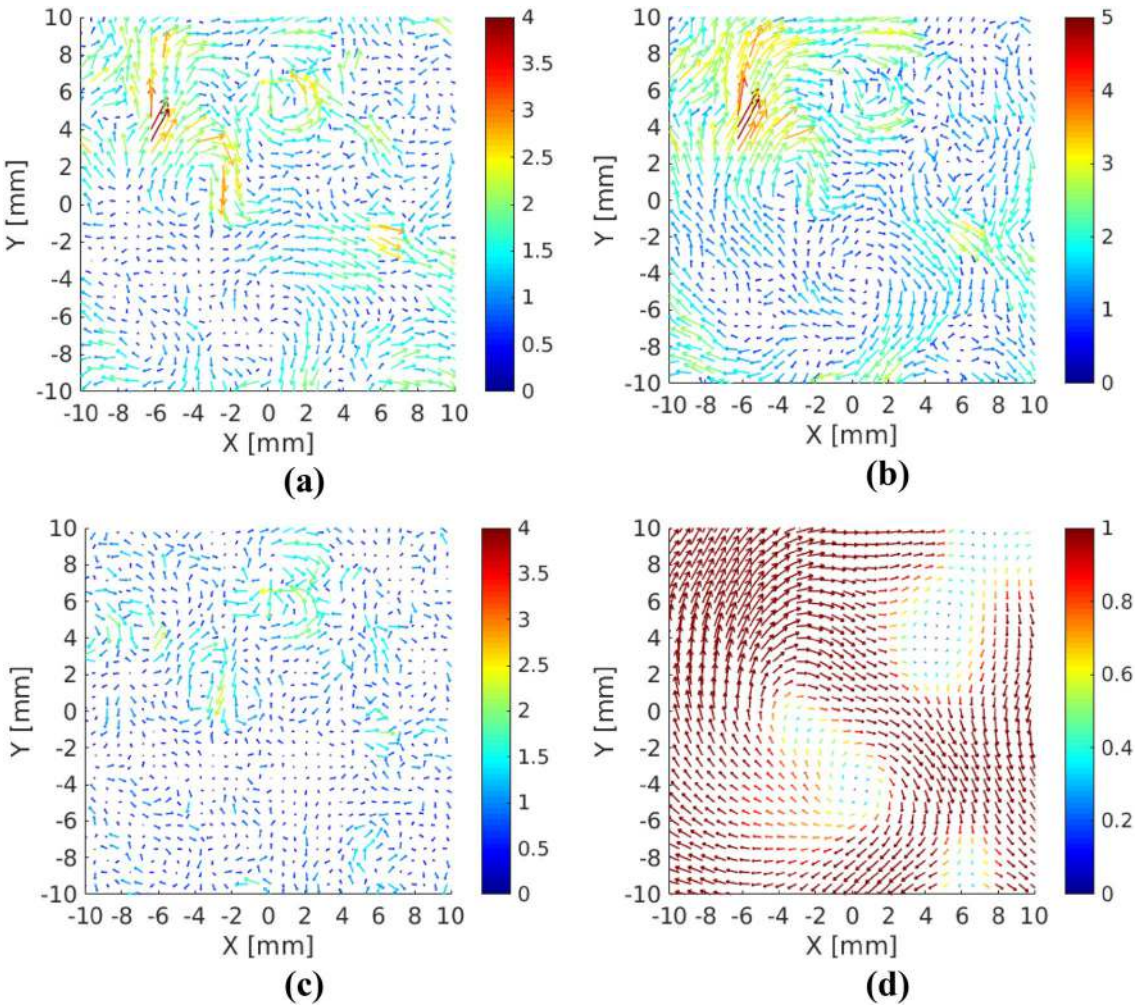

Fig. 17 Vortex amplitude $A = 1\,\mathrm{ms}^{-1}$, **a** initial HIT field 1; **b** perturbed velocity field; **c** recovered velocity field; **d** low-frequency part

spectra are underestimated for all the recovered fields. Furthermore, the relative mean square error between the added vortex and separated flow low-frequency part for the three under-study velocity fields is computed; for the case of vortex location in Fig. 17a, $\sigma = 4.1, 2, 3\%$ and for the vortex location in Fig. 17b, $\sigma = 6.8, 2.9, 4.7\%$.

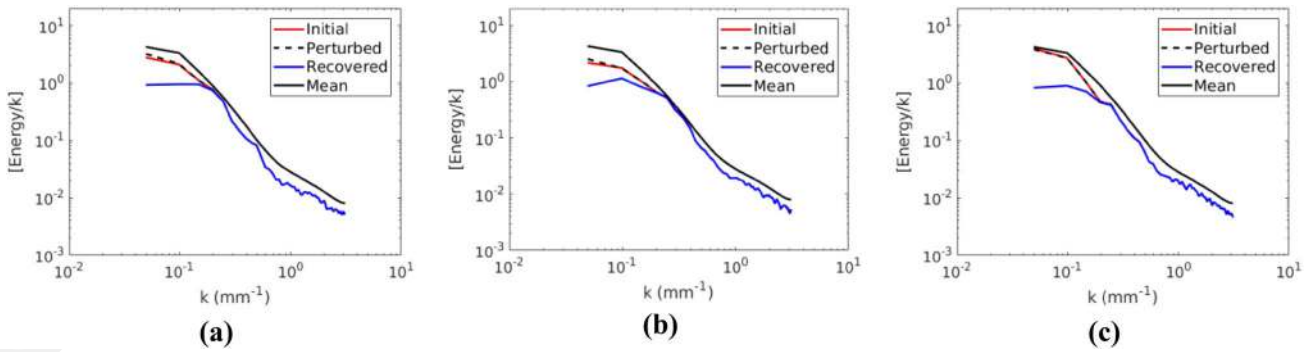

Fig. 18 $A = 1\,\mathrm{ms}^{-1}$, spatial power spectra of the initial HIT, perturbed and recovered velocity fields. **a** HIT field 1; **b** HIT field 2; **c** HIT field 3

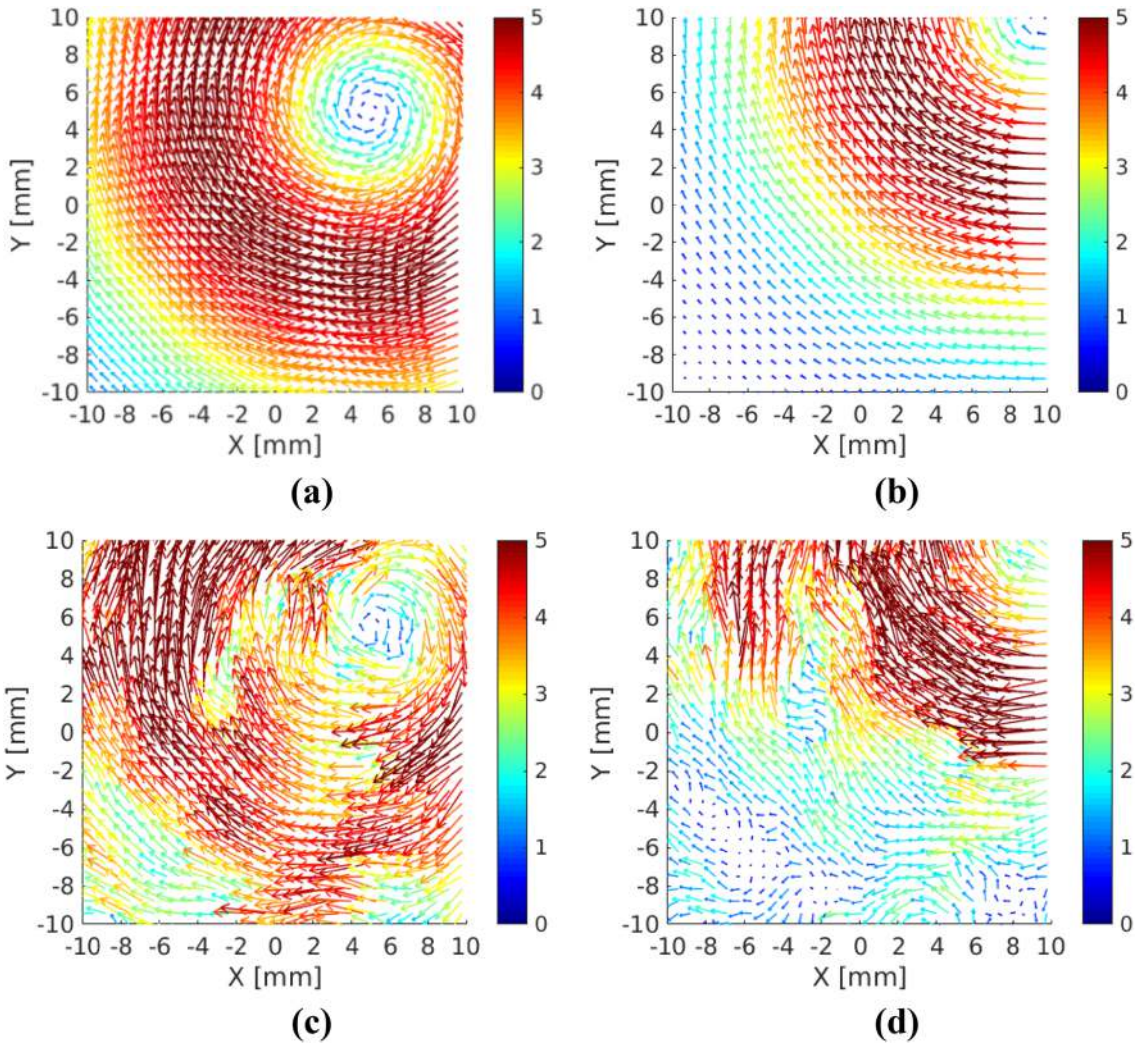

Fig. 19 **a**, **b** Perturbation vortices; **c**, **d** corresponding perturbed velocity fields

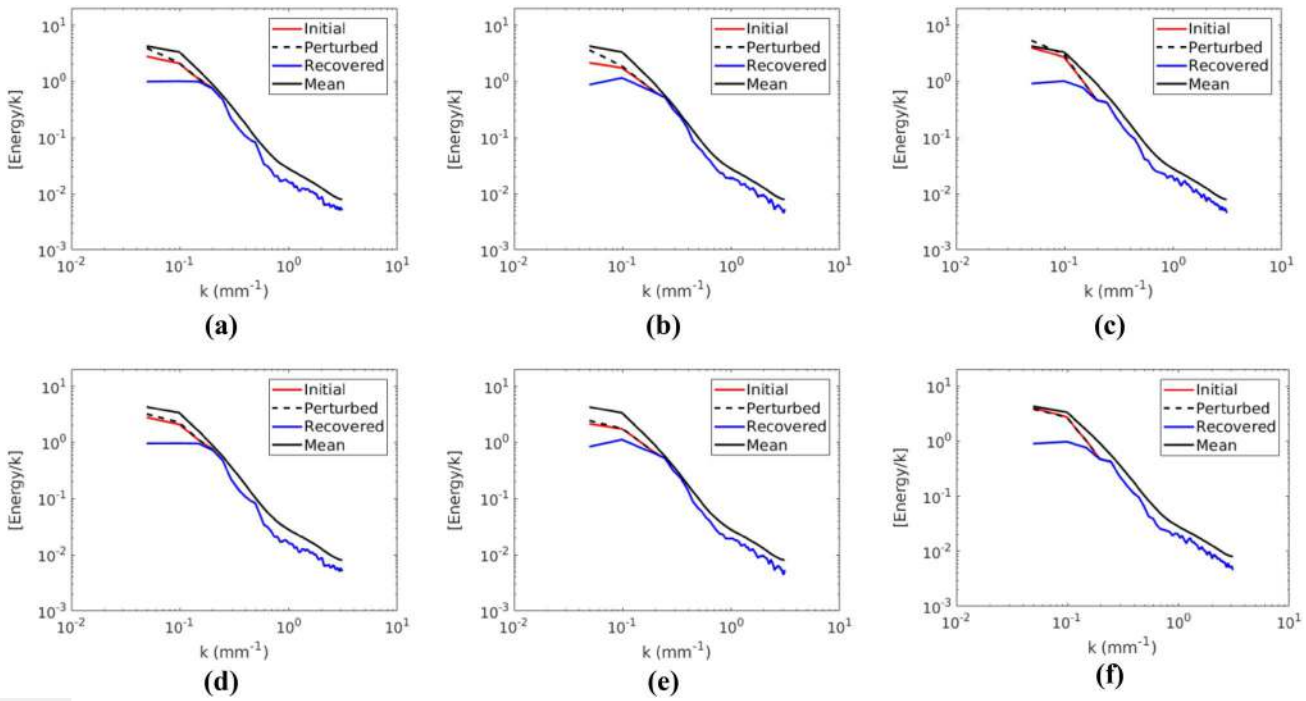

Fig. 20 Spatial power spectra of the initial HIT, perturbed and recovered velocity fields. Vortex location in Fig. 17a: **a** HIT field 1; **b** HIT field 2; **c** HIT field 3, vortex location in Fig. 17b: **d** HIT field 1; **e** HIT field 2; **f** HIT field 3

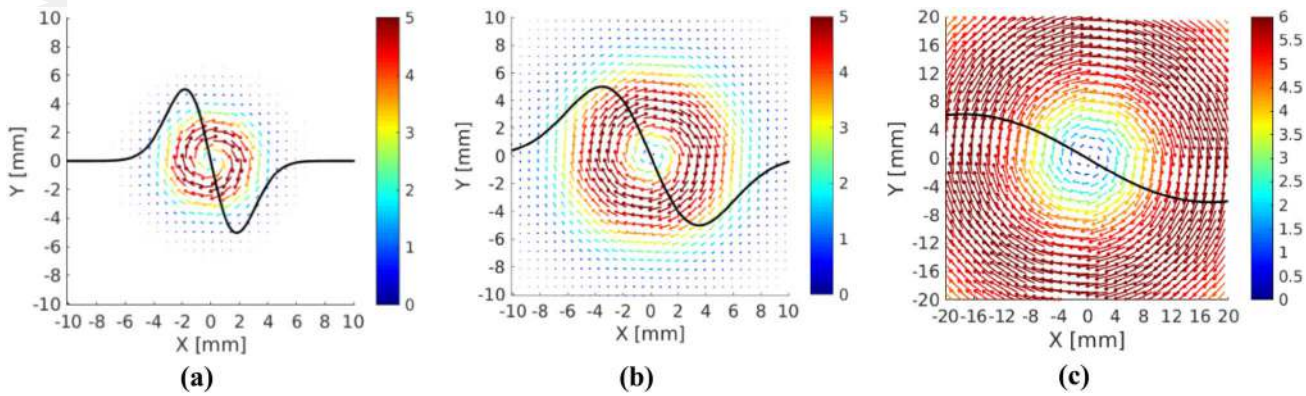

Fig. 21 Centered perturbation vortex of size **a** $l = 1 \cdot L_{(Ux,Vy)}$; **b** $l = 2 \cdot L_{(Ux,Vy)}$; **c** $l = 10 \cdot L_{(Ux,Vy)}$

4.3 Influence of the vortex size

The influence of the characteristic size of the perturbation on the quality of the recovered signal obtained after EMD analysis was then investigated. For this aim, the amplitude of the vortex was set to 5 $m\,s^{-1}$ and located at the center of the initial velocity field. The size l was varied as a function of the longitudinal integral length scale of the initial HIT flow: $l = \alpha \cdot L_{(Ux,Vy)}$ with $L_{(Ux,Vy)} = 3.2$ mm and $\alpha = 1, 2, 5$ and 10. The perturbation vortices generated with $\alpha = 1$, $\alpha = 2$ and $\alpha = 10$ (the amplitude was set to 6 ms^{-1}) are shown in Fig. 21; the case in which $\alpha = 5$ with $A = 10$ m s^{-1} is presented in Fig. 14.

The three HIT velocity fields were perturbed by these synthetic vortices. By applying the energy content criterion, the initial velocity fields are recovered. In these cases also, the jump in the energy contents occurred at the 5th mode. For a vortex size of $l = 10 \cdot L_{(Ux,Vy)}$, the results for

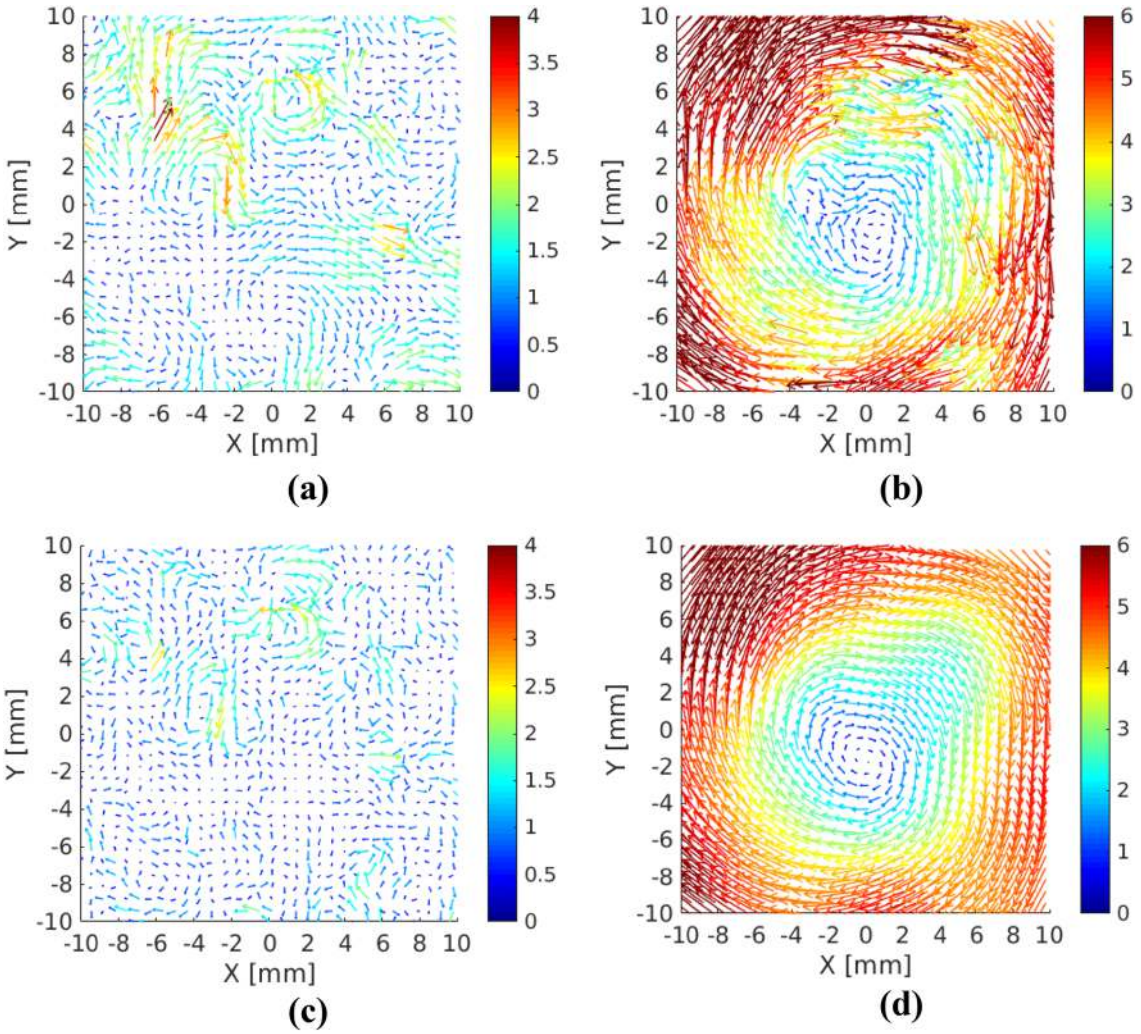

Fig. 22 Vortex size $l = 10L_{(Ux,Vy)}$, **a** initial HIT field 1; **b** perturbed velocity field; **c** recovered velocity field; **d** low frequency part

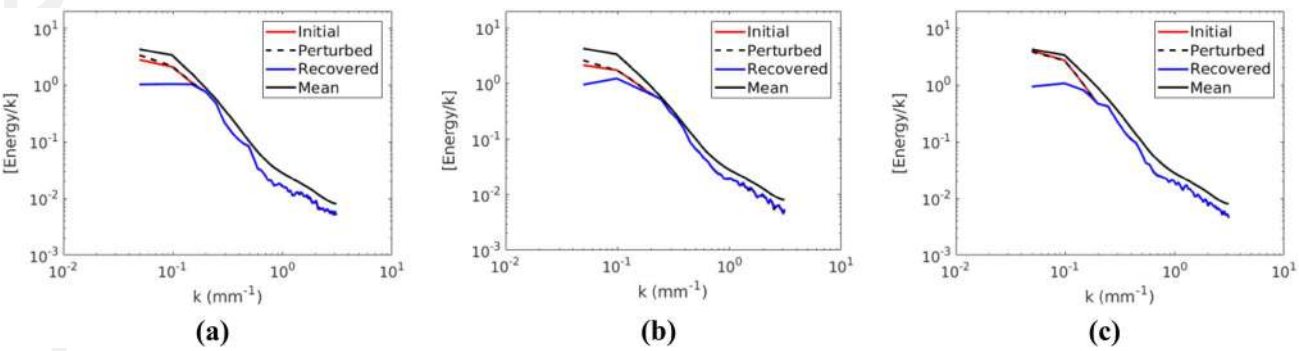

Fig. 23 Vortex size $l = 10L_{(Ux,Vy)}$, spatial power spectra of the initial HIT, perturbed and recovered velocity fields. **a** HIT field 1; **b** HIT field 2; **c** HIT field 3

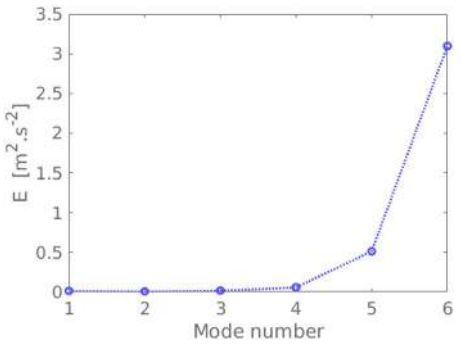

Fig. 24 Energy contents as a function of mode number, $l = 2 \cdot L_{(Ux,Vy)}$

HIT field 1 are presented in Fig. 22 as an example. The energy spectra of the initial HIT, perturbed and recovered velocity fields are also presented in Fig. 23. The results are similar to the previous cases and the recovering quality is not affected by the increase in the perturbation vortex scale with respect to the integral length scales of the initial HIT flows. Also in this case, $\sigma = 2.4, 1.9, 3.5\%$ for three under studies velocity fields.

In the case of $l = 2 \cdot \mathrm{L}_{(\mathrm{Ux,Vy})}$, the energy criterion for the result modes is plotted in Fig. 24. It is observed that the energy content does not jump strongly from the fifth to the sixth mode as in all the previous cases, but starts to evolve from the fourth mode. Therefore, the recovered turbulent flow was computed from the sum of the first five modes and the sixth mode was considered as an organized motion as presented in Fig. 25c, d. As can be seen, some signatures of the perturbation vortex appear in the center of the recovered turbulent velocity field. This feature also appears as an increase in the energy of the recovered velocity field compared to the initial HIT flow in the region of small wave numbers, see Fig. 26a.

To avoid some large-scale components on the recovered velocity field, the recovered field was considered as the sum of the first four modes as in Fig. 25e. Therefore, the corresponding low-frequency field, Fig. 25f, is more representative of the generated one. However, a severe shoot in the power spectral density of the recovered turbulent velocity field can be observed in Fig. 26b. It should be pointed out that the same results were obtained for the case in which $l = L_{(Ux,Vy)}$.

5 Discussion and conclusion

To assess the potential of the proposed bivariate 2D-EMD to separate large-scale organized motion from random turbulent fluctuations in an instantaneous velocity field, the combination of an experimental HIT flow and a synthetic Lamb–Oseen vortex that mimics the large-scale structure of the flow was used as a perturbed velocity field. The amplitude, position and scale of the synthetic vortex were varied with respect to the initial turbulent velocity field.

As the perturbed velocity field is decomposed by bivariate 2D-EMD in different modes, by applying an energy criterion on the modes, the initial HIT flow was separated from the synthetic perturbation. The proposed approach is not sensitive to the perturbation amplitude, when the amplitude of the added vortex is one, two or five times the TKE of the initial HIT flow, the power spectrum of the recovered velocity field is superimposed on the initial one in the turbulent inertial subrange and the smallest scales region of the flow. For a vortex amplitude ten times the TKE, some fluctuations in the energy spectrum of the recovered fields at the smallest scale were noted. However, due to the low energy in this region, they can be neglected.

To confirm this conclusion, in Fig. 27, the spatial power spectrum of the first and second initial HIT velocity fields and their recovered spectra obtained from the perturbed velocity fields with different perturbation amplitudes are compared. The perturbations are positioned at the center of the initial HIT velocity fields with a size of $l = 5 \cdot L_{(Ux,Vy)}$. As one can see there is good agreement between the spatial power spectra of the recovered velocity fields.

The initial HIT field 1 and its fields recovered from different perturbed velocity fields are presented together in Fig. 28. As one can see, similar structures can be clearly detected in different recovered velocity fields as compared to the initial HIT flow. The initial velocity field, see Fig. 28a, contains some large-scale structures, which disappear in all the recovered turbulent velocity fields. Consequently, the energy spectra of the turbulent recovered velocity field are attenuated in the region associated with the small wavenumbers.

Figure 29 presents the spatial power spectrum for the recovered velocity fields from HIT fields 1 and 3 that are perturbed by vortices located at the center, at middistance between the center and corner of the initial HIT velocity fields. As can be noted, the power spectra of all the different recovered velocity fields are superimposed, indicating that the location of the perturbation vortex (that simulates large-scale organized motion) in an HIT velocity field does not affect the recovered velocity fields

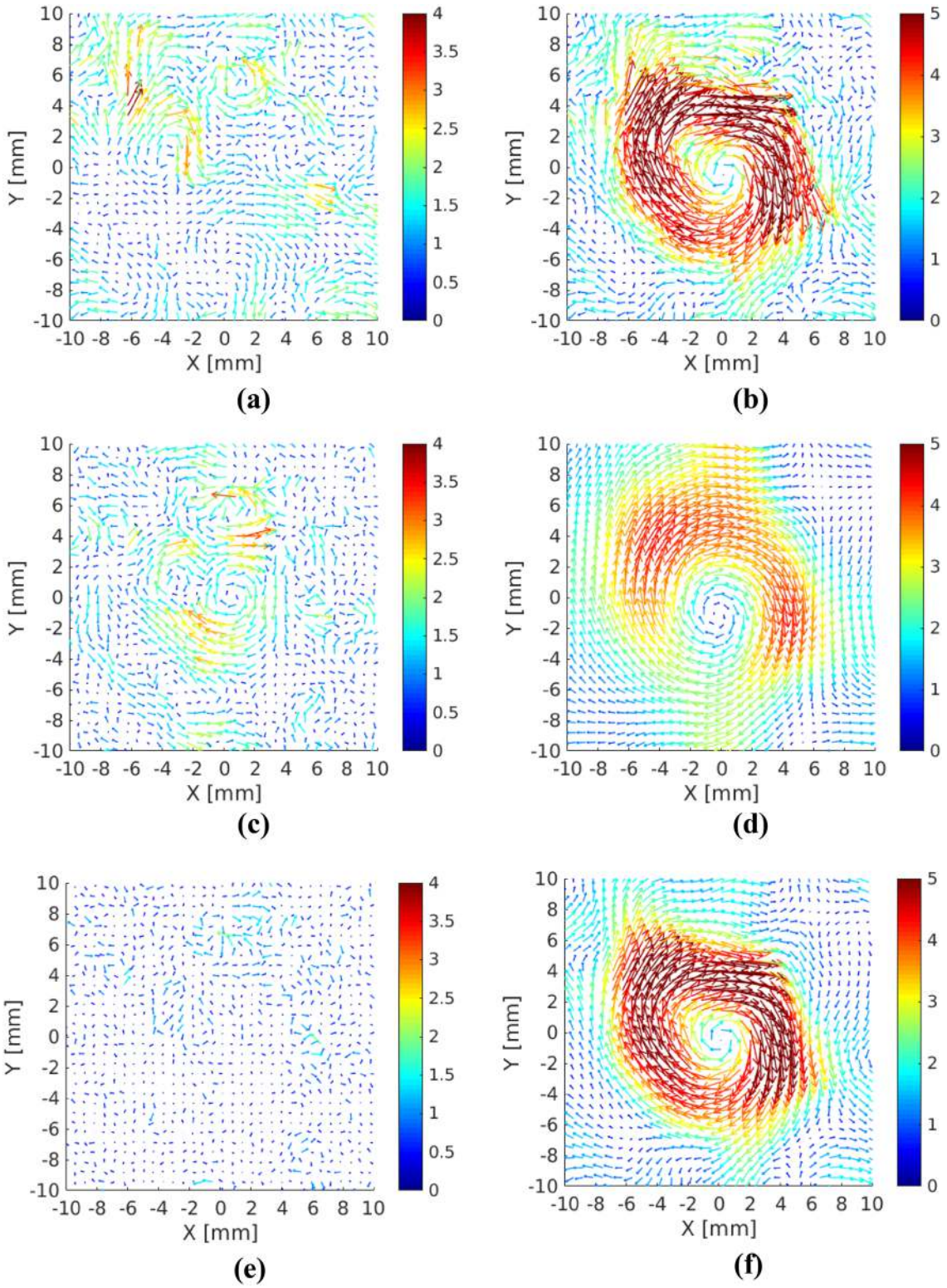

Fig. 25 Vortex size $l = 2 \cdot L_{(Ux,Vy)}$, **a** initial HIT field 1; **b** perturbed velocity field; **c** recovered from the first five modes and **d** low-frequency field, i.e., 6th mode; **e** recovered from the first four modes, **f** low frequency field, i.e., 5th+6th modes

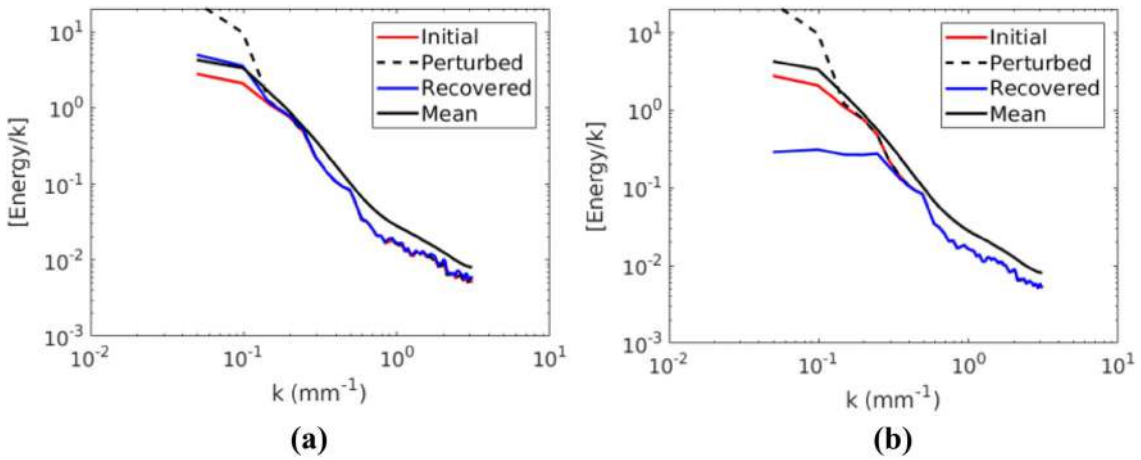

Fig. 26 Vortex size $l = 2L_{(Ux,Vy)}$, spatial power spectra of the initial HIT Field 1, perturbed and recovered velocity field. **a** Low-frequency component, i.e., 6th mode; **b** low frequency component, i.e., 5th+6th mode

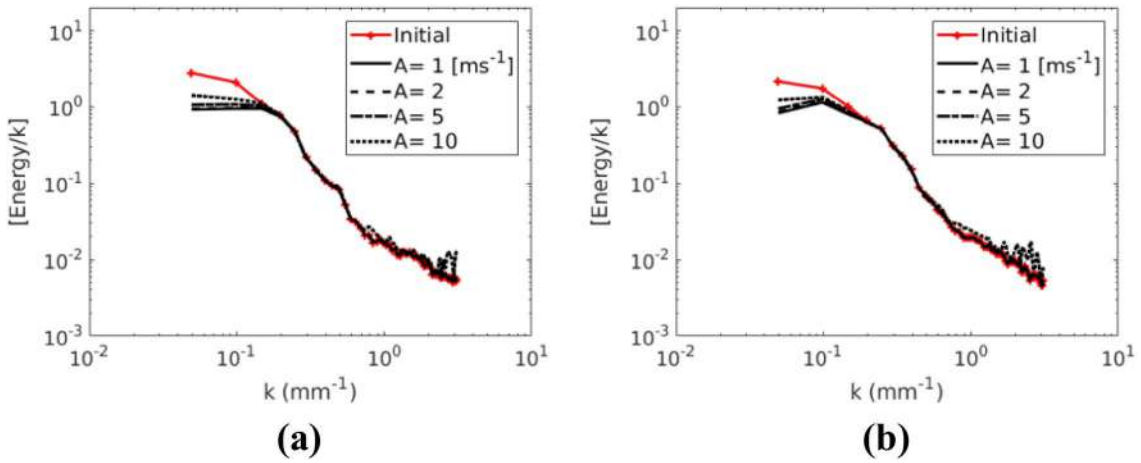

Fig. 27 Spatial power spectrum of the initial HIT velocity field and the recovered ones, obtained from the perturbed velocity fields with different vortex amplitudes. For **a** HIT field 1; **b** HIT field 2

that are obtained by bivariate 2D-EMD analysis. In addition, even when the center of the perturbation vortex is located at the boundary of the initial HIT velocity field, no over/under shoot effects exist at the borders of the resulting recovered velocity fields or at those in the low-frequency parts.

In addition, this investigation attests that when the size of the perturbation vortex is much larger than the integral length scale of the initial HIT flow, i.e., five or ten times $L_{(Ux,Vy)}$ that can be considered as a large-scale organized motion, the initial turbulent velocity field can be recovered using the bivariate 2D-EMD method with an energy criterion. However, when the size of the perturbation vortex approaches the turbulent length scale of the HIT flow, the quality of the recovered turbulent field is drastically reduced. When the size of the perturbation vortex is equal to the integral scale

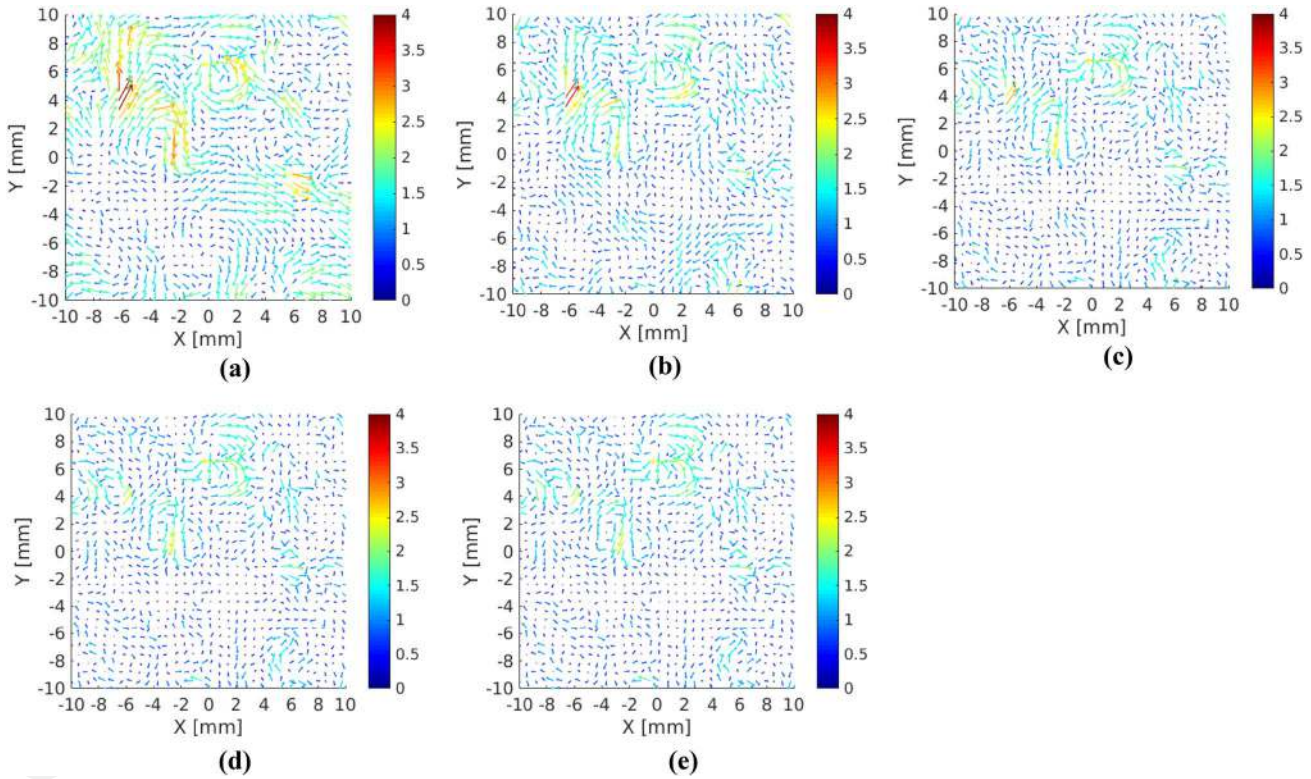

Fig. 28 **a** Initial HIT velocity field 1 versus recovered fields from perturbed fields with different vortex amplitudes A, **b** 10; **c** 5; **d** 2; **e** 1 m s^{-1}

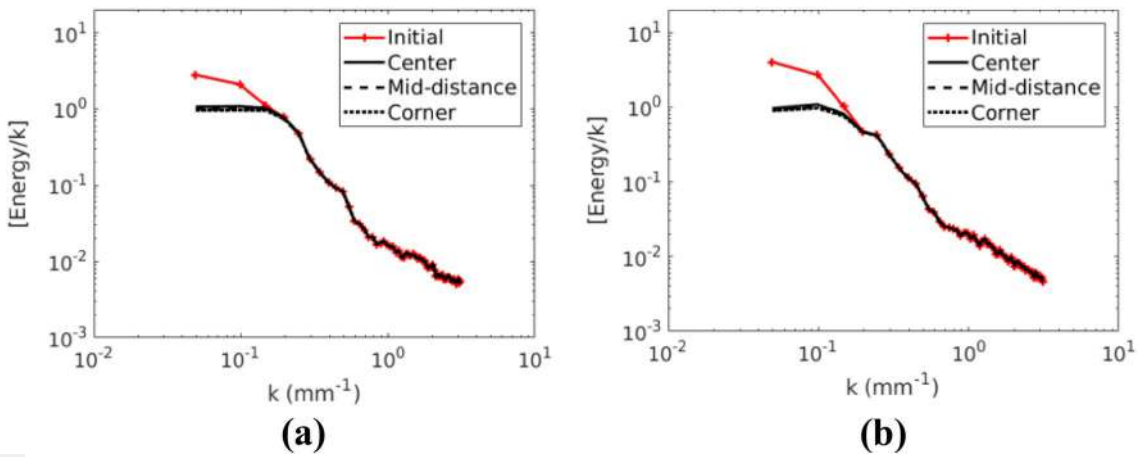

Fig. 29 Spatial power density spectrum of the initial HIT velocity field and the recovered turbulent velocity fields for different locations of the vortex center. **a** HIT field 1; **b** HIT field 2

of the initial velocity field $L_{(Ux,Vy)}$, they both have the same feature hence they are not detachable. It is interesting to point out that in bivariate 2D-EMD analysis, the separation between the organized motion and the turbulent fluctuations is not performed thanks to a cut-off frequency as in filtering approaches or thanks to the mode truncation order as in POD analysis. Figure 30a, b represents the evolution of the energy contents as a function of the mode number for the different amplitudes (with $l = 5 \cdot L_{(Ux,Vy)}$, the vortex is positioned at the center) and positions (with $l = 5 \cdot L_{(Ux,Vy)}$, $A = 5\,\mathrm{m\,s^{-1}}$) of the perturbation vortex, respectively. As one can see, in all cases perturbation is manifested as a sudden jump in the value of this criterion in the last mode (IMF), which in the bivariate 2D-EMD approach naturally has the lowest spatial frequency.

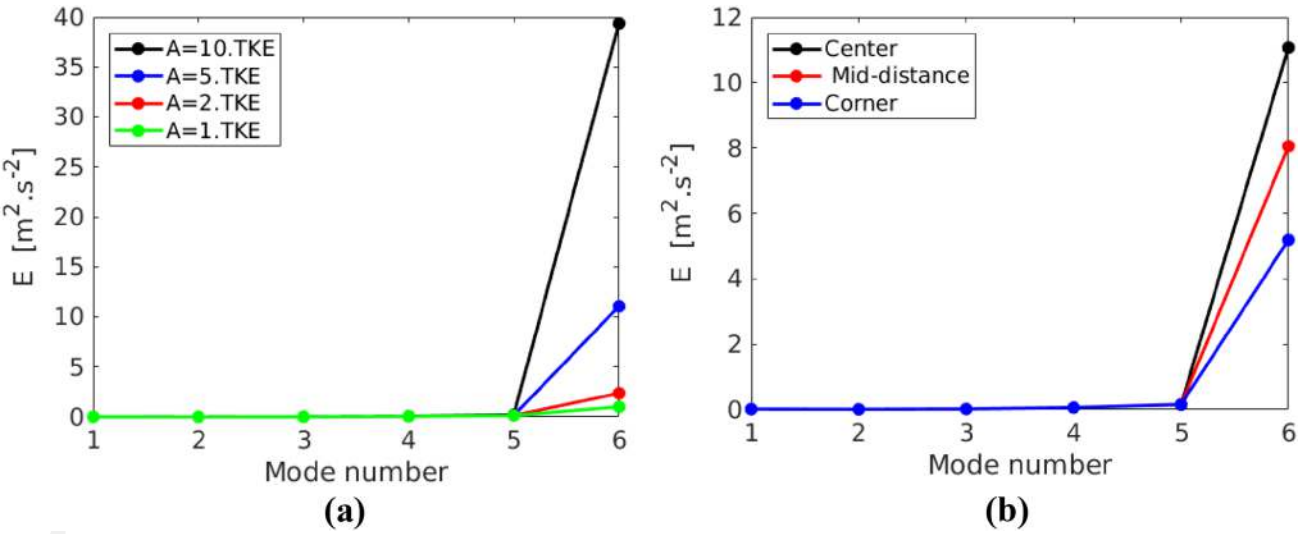

Fig. 30 Energy content for each mode. **a** Effect of the perturbation vortex amplitude; **b** effect of the vortex center location

From this study, it has been demonstrated that the major advantage of the bivariate 2D-EMD approach is that the turbulent part of a given instantaneous velocity field can be separated from organized motion based only on the instantaneous velocity field itself, whereas using the POD approach, this separation is performed based on several velocity fields to represent statistical averaging. This feature makes EMD a powerful tool for analyzing phenomena that are intrinsically transient. The proposed method is independent of the flow Reynolds number and can be used for analyzing 2D velocity fields obtained in different configurations such as in-cylinder flow, channel flow and flow above airfoils.

Acknowledgements This study was supported by the French National Research Agency through the ASTRIDE project. ANR-12-VPTT-0008.

Compliance with ethical standards

Conflict of interest The authors declare that they have no competing interests.

References

Ahrabian A, Rehman N, Mandic D (2013) Bivariate empirical mode decomposition for unbalanced real-world signals. IEEE Signal Process Lett 20(3):245–248

Bonnet JP, Delville J, Glauser MN, Antonia RA, Bisset DK, Cole DR, Fiedler HE, Garem JH, Hilberg D, Jeong J, Kevlahan NKR, Ukeiley L, Vincendeau E (1998) Collaborative testing of eddy structure identification methods in free turbulent shear flows. Exp Fluids 25:197–225

Borée J, Miles P (2014) In-Cylinder Flow. In: Crolla D, Foster DE, Kobayashi T, Vaughan N (eds) Encyclopedia of automotive engineering. Wiley, Chichester

Brown GL, Roshko A (1974) On density effects and large structure in turbulent mixing layers. J Fluid Mech 64(4):775–816

Druault P, Guibert P, Alizon F (2005) Use of proper orthogonal decomposition for time interpolation from PIV data. Exp Fluids 39(6):1009–1023

Ducoin A, Astolfi JA, Deniset F, Sigrist JF (2009) Computational and experimental investigation of flow over a transient pitching hydrofoil. Eur J Mech B Fluids 28(6):728–743

Epps B (2017) Review of vortex identification methods. In 55th AIAA aerospace sciences meeting, p 0989

Farge M, Schneider K, Kevlahan N (1999) Non-Gaussianity and coherent vortex simulation for two-dimensional turbulence using an adaptive orthogonal wavelet basis. Phys Fluids 11(8):2187–2201

Farge M, Pellegrino G, Schneider K (2001) Coherent vortex extraction in 3D turbulent flows using orthogonal wavelets. Phys Rev Lett 87(5):054501

Feynman J, Ruzmaikin A (2014) The centennial gleissberg cycle and its association with extended minima. J Geophys Res Space Phys 119(8):6027–6041

Fiedler HE (1998) Control of free turbulent shear flows. Flow control. Springer, Berlin, pp 335–429

Flandrin P (1998) Time-frequency/time-scale analysis, vol 10. Academic Press, Cambridge

Flandrin P, Rilling G, Goncalves P (2004) Empirical mode decomposition as a filter bank. Signal Process Lett IEEE 11(2):112–114

Foucher F, Ravier P (2010) Determination of turbulence properties by using empirical mode decomposition on periodic and random perturbed flows. Exp Fluids 49(2):379–390

Foucher F, Landry L, Halter F, Mounaïm-Rousselle C (2008) Turbulent flow fields analysis of a spark-ignition engine as function of the boosted pressure. In: 14th international symposium on laser techniques to fluid mechanics

Franzke CL (2014) Warming trends: nonlinear climate change. Nat Clim Change 4(6):423

Galmiche B, Mazellier N, Halter F, Foucher F (2014) Turbulence characterization of a high-pressure high-temperature fan-stirred

combustion vessel using LDV, PIV and TR-PIV measurements. Exp Fluids 55(1):1636
Guanlei X, Xiaotong W, Xiaogang X (2009) Improved bi-dimensional EMD and Hilbert spectrum for the analysis of textures. Pattern Recognit 42(5):718–734
Hemakom A, Ahrabian A, Looney D, Rehman NU, Mandic DP (2015) Nonuniformly sampled trivariate empirical mode decomposition. In: Acoustics, speech and signal processing (ICASSP) IEEE international conference on, pp 3691–3695
Hemakom A, Goverdovsky V, Looney D, Mandic DP (2016) Adaptive projection intrinsically transformed multivariate empirical mode decomposition in cooperative brain-computer interface applications. Philos Trans R Soc A Math Phys Eng Sci 374(2065):20150199
Hotelling H (1933) Analysis of a complex of statistical variables into principal components. J Educ Psychol 24(6):417
Huang NE, Attoh-Okine NO (2005) The Hilbert-Huang transform in engineering. CRC Press, Boca Raton
Huang NE, Shen Z, Lon SR, Wu MC, Shih HH, Zheng Q, Liu HH (1998) The empirical mode decomposition and the hilbert spectrum for nonlinear and non-stationary time series analysis. Proc R Soc Lond Ser A Math Phys Eng Sci 454(1971):903–995
Huang NE, Shen Z, Long SR (1999) A new view of nonlinear water waves: the Hilbert spectrum. Annu Rev Fluid Mech 31(1):417–457
Huang YX, Schmitt FG, Lu ZM, Liu YL (2008) An amplitude frequency study of turbulent scaling intermittency using empirical mode decomposition and Hilbert spectral analysis. EPL (Europhys Lett) 84(4):40010
Hussain AF (1983) Coherent structures—reality and myth. Phys Fluids 26(10):2816–2850
Lewalle J, Delville J, Bonnet JP (2000) Decomposition of mixing layer turbulence into coherent structures and background fluctuations. Flow Turbul Combust 64(9):301–328
Liang H, Lin QH, Chen JDZ (2005) Application of the empirical mode decomposition to the analysis of esophageal manometric data in gastroesophageal reflux disease. IEEE Trans Biomed Eng 52(10):1692–1701
Linderhed A (2009) Image empirical mode decomposition: a new tool for image processing. Adv Adapt Data Anal World Sci Publ Co 1(02):265–294
Looney D, Mandic DP (2009) Multiscale image fusion using complex extensions of emd. IEEE Trans Signal Process 57(4):1626–1630
Lumley JL (1967) The structure of inhomogeneous turbulent flows. In: Yalgom AM, Tatarski VI (eds) Atmospheric turbulence and wave propagation. Nauka, Moscow, pp 166–178
Lumley JL (2001) Early work on fluid mechanics in the IC engine. Annu Rev Fluid Mech 33(1):319–338
Mandic DP, Rehman N, Wu Z, Huang NE (2013) Empirical mode decomposition-based time-frequency analysis of multivariate signals: the power of adaptive data analysis. IEEE Signal Process Mag 30(6):74–86
Mazellier N, Foucher F (2011) Separation between coherent and turbulent fluctuations: what can we learn from the empirical mode decomposition? Exp Fluids 51(2):527–541
Nunes JC, Guyot Y, Delechelle E (2005) Texture analysis based on local analysis of the bidimensional empirical mode decomposition. Mach Vis Appl 16(3):177–188
Pearson K (1901) LIII. On lines and planes of closest fit to systems of points in space. Lond Edinb Dublin Philos Mag J Sci 2(11):559–572
Rehman N, Mandic DP (2009) Multivariate empirical mode decomposition. Proc R Soc A Math Phys Eng Sci 466(2117):1291–1302
Rehman N, Mandic DP (2010) Empirical mode decomposition for trivariate signals. IEEE Trans Signal Process 58(3):1059–1068
Rehman N, Mandic DP (2011) Filter bank property of multivariate empirical mode decomposition. IEEE Trans Signal Process 59(5):2421–2426
Rehman N, Looney D, Rutkowski TM, Mandic DP (2009) Bivariate EMD-based image fusion. In: Statistical signal processing, 2009. SSP'09. IEEE/SP 15th workshop on. IEEE, pp 57–60
Rehman N, Park C, Huang NE, Mandic DP (2013) EMD via MEMD: multivariate noise-aided computation of standard EMD. Adv Adapt Data Anal 5(02):1350007
Rehman N, Ehsan S, Abdullah SMU, Akhtar MJ, Mandic DP, McDonald-Maier KD (2015) Multi-scale pixel-based image fusion using multivariate empirical mode decomposition. Sensors 15(5):10923–11094
Reynolds WC, Hussain AKMF (1972) The mechanics of an organized wave in turbulent shear flow. Part 3. Theoretical models and comparisons with experiments. J Fluid Mech 54(2):263–288
Rilling G, Flandrin P, Goncalves P, Lilly JM (2007) Bivariate empirical mode decomposition. Signal Process Lett 14(12):936–939
Roudnitzky S, Druault P, Guibert P (2006) Proper orthogonal decomposition of in-cylinder engine flow into mean component, coherent structures and random Gaussian fluctuations. J Turbul 7:1–19
Sadeghi M, Foucher F, Abed-Meraim K, Mounaïm-Rousselle C (2016) Analysis of the bivariate EMD behavior for separating coherent structures from interference fluctuations in isotropic homogeneous turbulence. In: Progress in turbulence VI, pp 97–103
Schmid PJ (2010) Dynamic mode decomposition of numerical and experimental data. J Fluid Mech 656:5–28
Strang G (1989) Wavelets and dilation equations: a brief introduction. SIAM Rev 31(4):614–627
Wang G, Chen XY, Qiao FL, Wu Z, Huang NE (2010) On intrinsic mode function. Adv Adapt Data Anal 2(03):277–293
Wang YH, Yeh CH, Young HWV, Hu K, Lo MT (2014) On the computational complexity of the empirical mode decomposition algorithm. Phys A 400:159–167
Wu Z, Huang NE (2004) A study of the characteristics of white noise using the empirical mode decomposition method. Proc R Soc Lond Ser A Math Phys Eng Sci 460(2046):1597–1611
Wu Z, Huang NE (2009) Ensemble empirical mode decomposition: a noise assisted data analysis method. Adv Adapt Data Anal 1(01):1–41
Wu Z, Huang NE, Chen X (2009) The multi-dimensional ensemble empirical mode decomposition method. Adv Adapt Data Anal 1(03):339–372
Wu CH, Chang HC, Lee PL, Li KS, Sie JJ, Sun CW, Yang C, Li PH, Deng HT, Shyu KK (2011) Frequency recognition in an SSVEP-based brain computer interface using empirical mode decomposition and refined generalized zero-crossing. J Neurosci Methods 196(1):170–181
Zhou Y, Chen W, Gao J, He Y (2012) Application of Hilbert–Huang transform based instantaneous frequency to seismic reflection data. J Appl Geophys 82:68–74